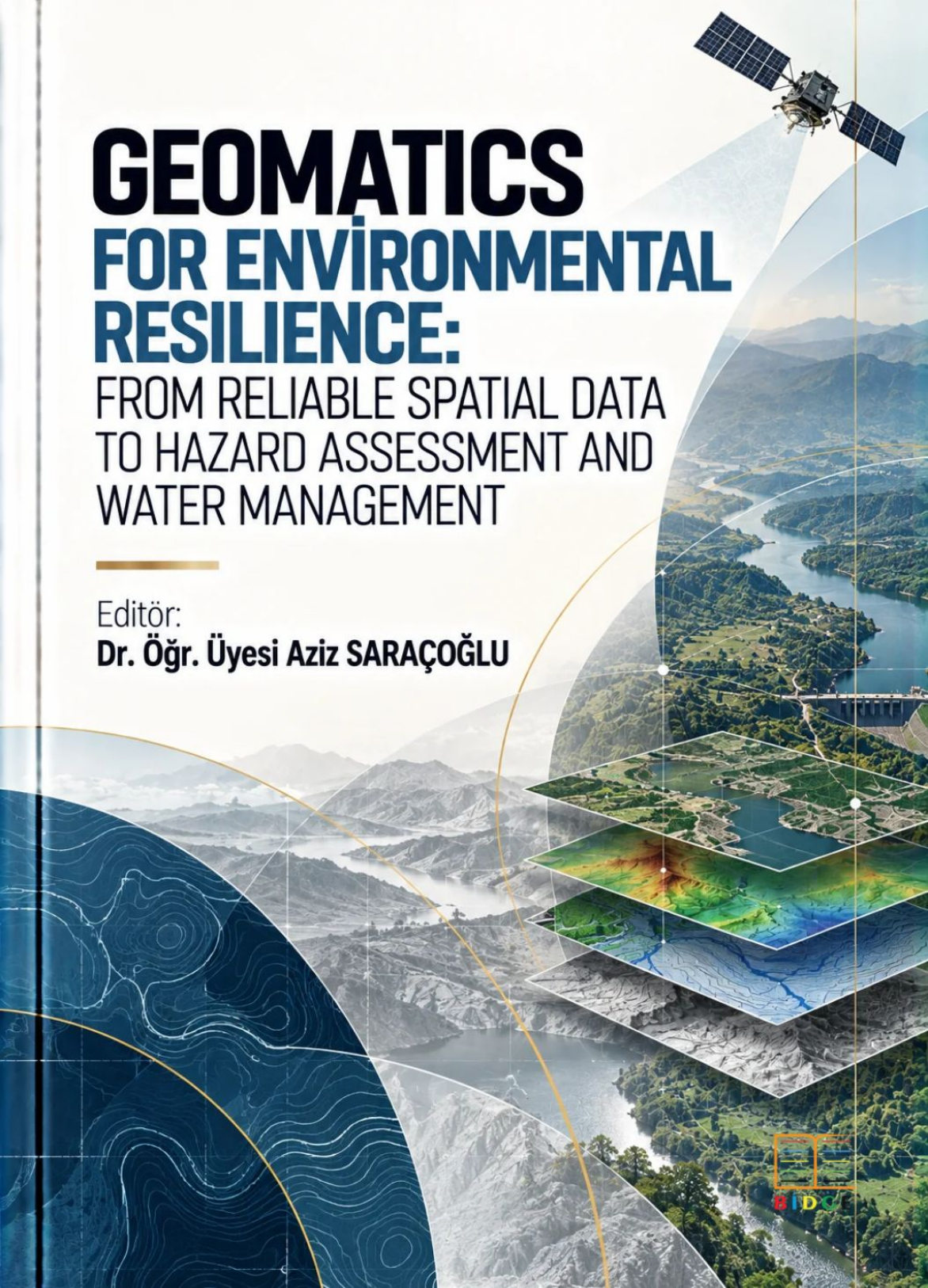
# GEOMATICS FOR ENVİRONMENTAL RESILIENCE:

## FROM RELIABLE SPATIAL DATA TO HAZARD ASSESSMENT AND WATER MANAGEMENT

Editör:
**Dr. Öğr. Üyesi Aziz SARAÇOĞLU**



**BİDGE Yayınları**

**Geomatics For Environmental Resilience: From Reliable Spatial Data To Hazard Assessment and Water Management**

**Editör:** Dr. Öğr. Üyesi Aziz SARAÇOĞLU

**ISBN:** 978-625-5474-80-3

1. Baskı
Sayfa Düzeni: Gözde YÜCEL
Yayınlama Tarihi: 2026-10-25
BİDGE Yayınları

Bu eserin bütün hakları saklıdır. Kaynak gösterilerek tanıtım için yapılacak kısa alıntılar dışında yayıncının ve editörün yazılı izni olmaksızın hiçbir yolla çoğaltılamaz.

Sertifika No: 71374
Yayın hakları © BİDGE Yayınları
www.bidgeyayinlari.com.tr - bidgeyayinlari@gmail.com
Krc Bilişim Ticaret ve Organizasyon Ltd. Şti.
Güzeltepe Mahallesi Abidin Daver Sokak Sefer Apartmanı No: 7/9 Çankaya / Ankara

# PREFACE

Geomatics has become a key discipline for transforming spatial observations into reliable knowledge in a world increasingly shaped by natural hazards and environmental pressures. This book, titled **“Geomatics For Environmental Resilience: From Reliable Spatial Data To Hazard Assessment and Water Management”**, explores this transformation by connecting the production of accurate spatial data with the analysis of natural hazards and the planning of water resources. It highlights that the value of geospatial information lies not only in the precision with which it is acquired but also in its capacity to support informed decisions on disaster preparedness, water security, and sustainable land use.

Addressing pressing challenges such as seismic hazards, drought, and the growing pressure of climate change on water resources, this volume presents a coherent pathway from data reliability to evidence-based decisions. The chapters examine how Unmanned Aerial Vehicle (UAV) photogrammetry, elevation models, and LiDAR help minimize geometric distortions, and how Geographic Information Systems (GIS) are combined with spatial statistics, the Analytical Hierarchy Process (AHP), and satellite-based drought indices. These tools are applied across diverse settings, from complex urban and densely vegetated landscapes to the century-long seismic record of Türkiye and the identification of suitable areas for rainwater harvesting. This structure reflects the progression of spatial data from a precise measurement to a solid foundation for disaster risk reduction and sustainable water management.

I hope this book serves as a useful reference for academics, researchers, and practitioners, and encourages further interdisciplinary studies at the intersection of geomatics, natural hazards, and water resources. I would like to extend my sincere thanks to all the authors for their valuable contributions, the reviewers for their careful evaluations, and the publishing staff for their support in bringing this volume to life.

Sincerely,

Assist. Prof. Dr. AZİZ SARAÇOĞLU

FIRAT UNIVERSITY

# İÇİNDEKİLER

GEOMETRIC DISTORTIONS IN SPATIAL PRODUCTS DERIVED FROM AERIAL PHOTOGRAPHS: CAUSES, ELEVATION MODEL DEPENDENCY, AND IMPROVEMENT STRATEGIES ..... 1

*MÜGE AĞCA, NİLÜFER ÖZDAŞ*

SPATIAL-STATISTICAL EVALUATION OF EARTHQUAKE ACTIVITIES IN TÜRKIYE ..... 25

*RAMAZAN GÜNGÖR*

DETERMINATION OF SUITABLE AREAS FOR RAINWATER HARVESTING AND DROUGHT ANALYSIS IN DEMIRCI DISTRICT ..... 52

*RAMAZAN GÜNGÖR*

# BÖLÜM 1

# GEOMETRIC DISTORTIONS IN SPATIAL PRODUCTS DERIVED FROM AERIAL PHOTOGRAPHS: CAUSES, ELEVATION MODEL DEPENDENCY, AND IMPROVEMENT STRATEGIES

**MÜGE AĞCA**[1]
**NİLÜFER ÖZDAŞ**[2]

## Introduction

The growing demand for high-resolution geospatial information has significantly influenced contemporary mapping and spatial analysis practices. In this context, aerial photogrammetry has become one of the most widely used methods for acquiring spatial data. Advances in digital camera systems, image processing techniques, and unmanned aerial vehicle (UAV) technologies have made it possible to obtain highly detailed representations of physical environments in a relatively rapid and efficient manner. While aerial photographs were once used mainly for military reconnaissance and

[1] Doç. Dr., İzmir Katip Çelebi Üniversitesi, Harita Mühendisliği Bölümü, Orcid: 0000-0003-0190-7280
[2] Arş. Gör., İzmir Katip Çelebi Üniversitesi, Harita Mühendisliği Bölümü, Orcid: 0009-0007-3929-6813

topographic mapping, they are now applied in many different fields, including engineering, environmental monitoring, urban planning, disaster management, precision agriculture, and infrastructure studies (Jiang et. al., 2021; Gonçalves et. al., 2021). As a result, spatial products generated from aerial imagery have become an essential component of geomatics engineering and many related disciplines.

The integration of UAV systems into photogrammetric workflows has also changed how spatial data are produced and accessed. Compared to conventional manned aerial surveys and satellite-based approaches, UAVs provide several practical advantages such as lower operational costs, flexible flight planning opportunities, and very high spatial resolution. In addition, UAV platforms make it possible to collect imagery under different acquisition geometries depending on project requirements. This flexibility has contributed to the wider use of Structure-from-Motion (SfM) and Multi-View Stereo (MVS) techniques, which allow the reconstruction of dense three-dimensional (3D) models from overlapping photographs captured from multiple viewpoints (Morgan et. al., 2019). Through these approaches, orthophotos, digital elevation models, dense point clouds, textured meshes, and realistic 3D spatial representations can be generated in a relatively efficient and cost-effective way.

Despite these developments, spatial products derived from aerial imagery are still affected by several geometric and radiometric distortions that may reduce positional accuracy and reliability. Many of these problems originate from the central projection geometry of aerial imaging systems. Objects located above the terrain surface may appear differently depending on their elevation, distance from the image center, and viewing angle. In addition, variations in terrain characteristics, sensor orientation, illumination conditions, and environmental complexity may further complicate the production of

geometrically accurate outputs and orthorectified products (Liu et. al., 2021).

Among the many factors influencing aerial image-based spatial products, high vertical structures and dense vegetation are generally considered among the most challenging conditions. In urban areas, high-rise buildings, industrial facilities, towers, and compact urban blocks often lead to radial displacement, occlusion, shadow effects, and perspective-related deformations. These effects may distort object geometry and limit the visibility of ground-level details. Similarly, densely vegetated environments create important limitations for terrain reconstruction because vegetation canopy may obstruct the actual ground surface. This situation can reduce the accuracy of Digital Terrain Models (DTMs), affect image matching quality, and introduce radiometric inconsistencies into photogrammetric outputs (Amhar et. al., 1998; Murtiyoso et. al., 2017). Consequently, geometric fidelity and positional consistency may decrease substantially in such environments.

Understanding the causes and implications of these distortions is important not only from a technical perspective but also for practical applications. Errors in orthophotos or elevation models may directly affect engineering projects, cadastral studies, flood simulations, environmental risk assessments, and urban planning decisions. For example, insufficient correction of building lean in urban orthophotos may produce positional inaccuracies that influence land administration and infrastructure management. In vegetated environments, elevation errors beneath tree canopies may lead to misleading hydrological analyses or slope estimations (Trepekli et. al., 2022). For this reason, producing spatial data with engineering-level accuracy requires more than high-resolution imagery alone. Appropriate image acquisition strategies, reliable elevation models, and suitable correction procedures are equally important.

To reduce these limitations, contemporary photogrammetric workflows increasingly incorporate various correction strategies and supporting technologies. These include the use of high-resolution elevation models, true orthophoto production, multi-view image acquisition, radiometric enhancement methods, seamline optimization, and active remote sensing approaches such as LiDAR. In particular, the selection and quality of DTMs and Digital Surface Models (DSMs) play an important role in minimizing geometric distortions and improving the accuracy of final products (Arrighi & Campo, 2019). In recent years, developments in machine learning methods and automated image correction techniques have also contributed to improving the quality of UAV-based photogrammetric products in geometrically complex environments (Varshosaz et. al., 2024).

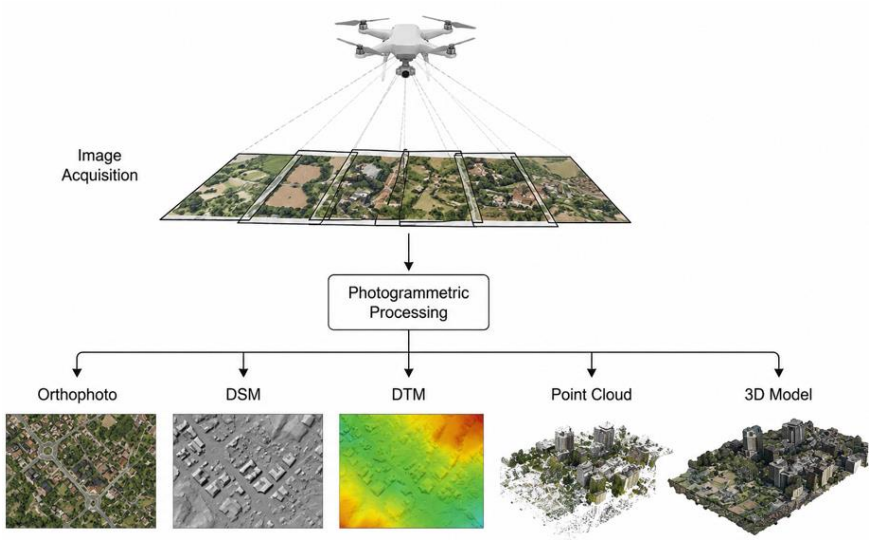
This chapter examines the distortions observed in spatial products generated from aerial photographs and discusses possible approaches to reduce their impacts, particularly in areas containing high vertical structures and dense vegetation. Special attention is given to the contribution of elevation models, including DTMs and DSMs, to improving geometric consistency and orthorectification performance. The chapter first introduces the role of aerial photography in cartographic applications and three-dimensional modeling workflows. It then discusses the main mechanisms responsible for geometric distortions and reviews several technological and methodological developments, including true orthophoto generation, radiometric enhancement, seamline optimization, multi-view image acquisition, and LiDAR-assisted elevation modeling. Finally, recent improvements aimed at increasing the reliability of photogrammetric products are evaluated in light of current literature.

## Aerial Photographs and Mapping

Aerial photographs have long been one of the primary data sources used in mapping and geospatial data production. In general terms, they are images captured from elevated platforms such as aircraft or UAVs, offering a broad perspective of the Earth's surface and enabling the collection of detailed spatial information over relatively large areas within a short time. In geomatics engineering, the role of aerial imagery has gradually expanded beyond simple visual documentation and become an essential component of topographic mapping, orthophoto production, 3D city modelling, terrain analysis, environmental monitoring, and disaster management studies (Jiang et. al., 2021). Particularly with the increasing use of UAV technologies, aerial photogrammetry has become more accessible due to lower operational costs, flexible data acquisition opportunities, and the ability to produce ultra-high-resolution imagery (Murtiyoso et. al., 2017).

The importance of aerial photographs in mapping is closely related to their ability to represent terrain geometry through photogrammetric principles. Unlike conventional terrestrial surveying methods, which often require intensive field measurements and longer data acquisition periods, aerial imagery enables the rapid and systematic collection of information over extensive regions. Following data acquisition, these images are processed through photogrammetric workflows to produce measurable geospatial outputs such as orthophotos, DSM, DTM, contour maps, and three-dimensional digital twins. As presented in Figure 1, aerial photographs form the basis of a wide range of geospatial applications extending from engineering projects to urban planning and environmental monitoring (Jiang et. al., 2021).

*Figure 1 General workflow and products of UAV-based aerial photogrammetry*

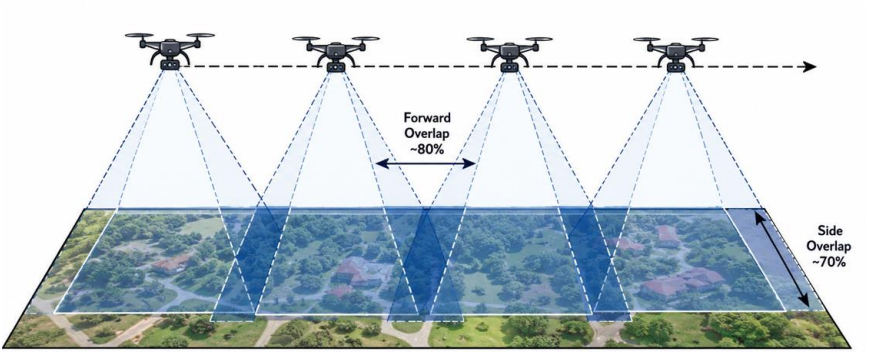



In recent years, the production of three-dimensional spatial information from aerial photographs has increasingly relied on SfM and MVS algorithms. The SfM approach reconstructs terrain or object geometry by identifying corresponding points within multiple overlapping photographs taken from different viewpoints. In many respects, this process resembles the stereoscopic depth perception mechanism of human vision. Through mathematical optimization, camera positions and object geometry are estimated simultaneously, allowing three-dimensional information to be reconstructed from ordinary two-dimensional photographs with a high level of geometric precision (Gonçalves et. al., 2021).

A key factor affecting the success of photogrammetric reconstruction is image overlap. During UAV-based image acquisition, flight plans are generally designed so that the same ground features appear in multiple photographs from different perspectives. To improve feature matching accuracy and overall model quality, forward overlap rates of approximately 80% and side overlap rates of around 70% are commonly recommended (Róg & Rzonca, 2021). When overlap levels are insufficient, problems such

as weak camera calibration, incomplete point cloud generation, and lower positional accuracy may occur. For this reason, flight planning is considered one of the important stages of UAV-based photogrammetric studies. The overlap geometry commonly applied in UAV photogrammetry is illustrated in Figure 2.

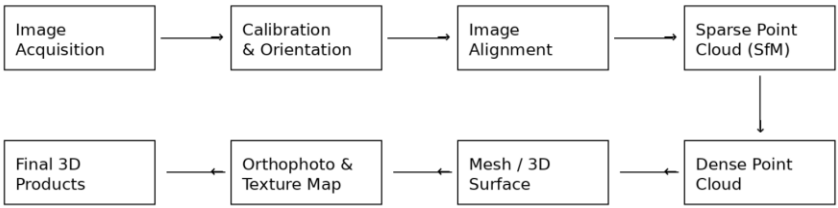
*Figure 2 Overlap principle in UAV photogrammetry*




*Róg & Rzonca (2021).*

Following image acquisition, the collected photographs are processed using photogrammetric software packages such as Agisoft Metashape, Pix4Dmapper, and RealityCapture. During processing, image alignment procedures identify common points between photographs and estimate camera positions together with their orientations. This stage produces a sparse point cloud, which represents the preliminary geometry of the terrain or object surface. In subsequent stages, dense image matching techniques generate a dense point cloud consisting of millions of georeferenced points. These data are later transformed into surface meshes and textured three-dimensional models (Morgan et. al., 2019). Finally, outputs such as orthophotos, DSMs, and DTMs are generated, providing measurable and georeferenced representations of the Earth's surface. The overall SfM-based photogrammetric workflow is shown in Figure 3.

*Figure 3 SfM-based aerial photogrammetric workflow*




Overall, aerial photographs have become an indispensable component of modern mapping practices because they provide spatial information in a relatively rapid, practical, and cost-effective way. UAV-supported photogrammetric approaches combined with SfM-MVS algorithms have considerably improved the production of high-resolution spatial models used in engineering, environmental monitoring, urban planning, and hazard assessment studies. Nevertheless, several factors, including terrain variability, dense vegetation, and high-rise structures, may still influence geometric accuracy. Therefore, understanding the basic principles behind aerial image acquisition and photogrammetric processing remains important for producing reliable spatial products.

## Geometric Distortion Mechanisms in Complex Landscapes: The Influence of High Structures and Dense Vegetation

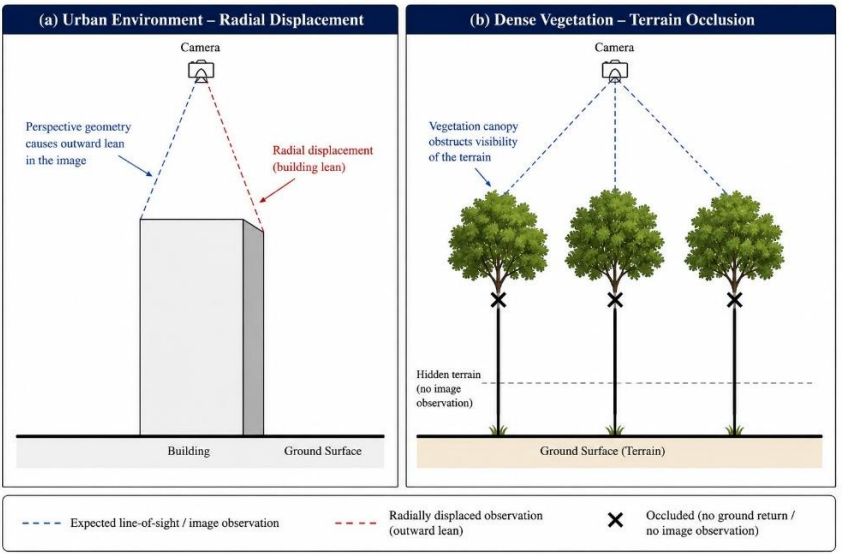
Spatial products generated from aerial photographs are often affected by various geometric distortions arising from terrain characteristics, image acquisition geometry, sensor limitations, and constraints associated with photogrammetric processing. Unlike orthographic projections, aerial photographs are produced through a central perspective projection system, where objects located at different elevations appear with varying degrees of geometric displacement. As a result, distortions become particularly noticeable in urban areas containing high-rise structures and in densely

vegetated environments where the terrain surface is partially or entirely obscured (Liu et. al., 2021; Murtiyoso et. al., 2017).

Among the key factors influencing geometric accuracy, high vertical structures and dense vegetation cover stand out due to their direct impact on image matching procedures and their tendency to introduce systematic positional uncertainties into photogrammetric outputs. In urban settings, tall buildings frequently cause radial displacement, occlusion, and shadow-related information loss, which may result in distorted orthophotos and inaccuracies in building footprints. Likewise, dense vegetation complicates terrain reconstruction by restricting ground visibility, often leading to elevation inaccuracies and increased noise in point cloud generation (Amhar et. al., 1998; Jiang et. al., 2021).

As illustrated in Figure 4, geometric distortions largely emerge through the interaction between image acquisition geometry and topographic complexity. Because of perspective geometry, high-rise buildings tend to lean outward from the image center, whereas tree canopies obstruct the direct visibility of the underlying terrain, limiting accurate extraction of the ground surface.

*Figure 4 Major sources of geometric distortions in aerial photogrammetry*

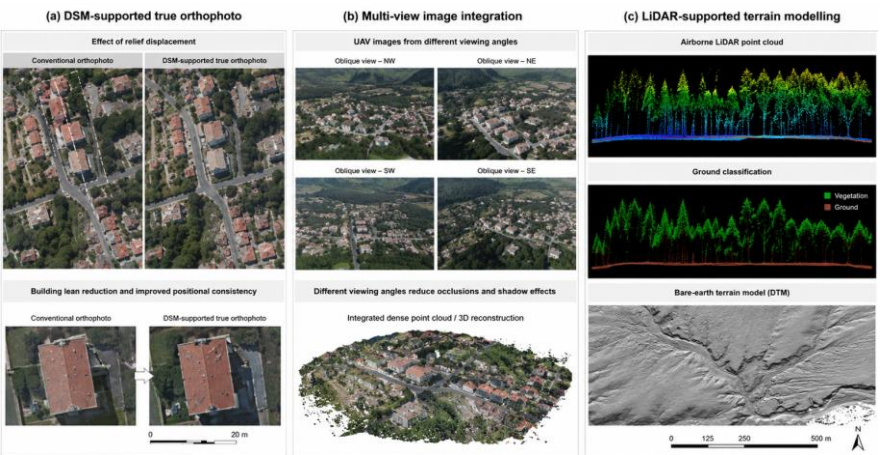



The severity of these distortions is strongly influenced by the type and quality of the elevation model applied during orthorectification and spatial product generation. Conventional DTM represent only the bare-earth surface and therefore have limitations in accurately modelling urban areas characterized by high-rise structures. By comparison, DSM incorporate above-ground objects, including buildings and vegetation, providing a more realistic representation of complex environments and helping to reduce positional errors associated with vertical discontinuities (Trepekli et. al., 2022).

Several improvement approaches have been introduced in contemporary photogrammetry to reduce geometric inaccuracies. One widely adopted strategy is the production of True Orthophotos, which utilize DSM-based orthorectification techniques to reduce building lean and improve positional consistency in urban areas (Rau et. al., 2002). Furthermore, multi-view image acquisition enhances visibility in occluded regions by integrating observations from multiple viewing angles, while radiometric enhancement methods,

such as histogram equalization, help reduce information loss in shadowed areas (Łabędź et. al., 2021). In densely vegetated landscapes, active remote sensing technologies such as LiDAR have proven particularly effective because of their ability to penetrate canopy cover and provide accurate ground elevation information (Varshosaz et. al., 2024). The relationship between distortion mechanisms, elevation models, and mitigation approaches is summarized in Figure 5.

*Figure 5 Improvement approaches for minimizing photogrammetric distortions*




*Rau et. al. (2002), Łabędź et. al. (2021), and Varshosaz et. al. (2024).*

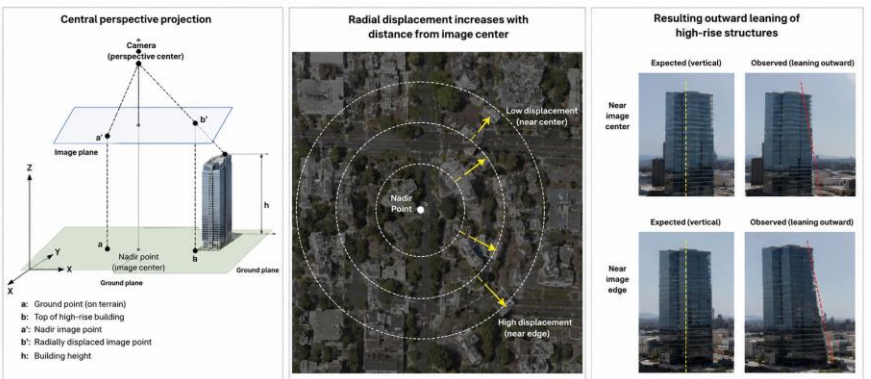
This chapter specifically addresses distortions associated with high vertical structures and dense vegetation cover by discussing their underlying causes, the role of elevation models in reducing inaccuracies, and current methodological approaches aimed at improving spatial accuracy in aerial photogrammetric products.

## Distortion Caused by High Vertical Structures and Their Underlying Causes

High-rise buildings, towers, chimneys, bridges, and similar vertical structures are among the most prominent sources of geometric distortion in aerial photogrammetry. Because aerial imagery is acquired using a central perspective projection, objects positioned above the ground surface tend to be displaced radially away from the nadir point of the image. This effect, commonly known as radial displacement, becomes more pronounced as both building height and distance from the image center increase (Liu et. al., 2021). As a consequence, tall structures often appear to lean outward rather than remain vertically aligned, introducing inaccuracies into building footprints and orthophoto representations.

As illustrated in Figure 6, the impact of radial displacement is particularly evident in dense urban areas, where pronounced vertical discontinuities intensify the apparent outward leaning of buildings toward the edges of the image.

*Figure 6 Radial displacement effect caused by high-rise structures in aerial imagery*




*Liu et. al. (2021) and Dai et. al. (2011).*

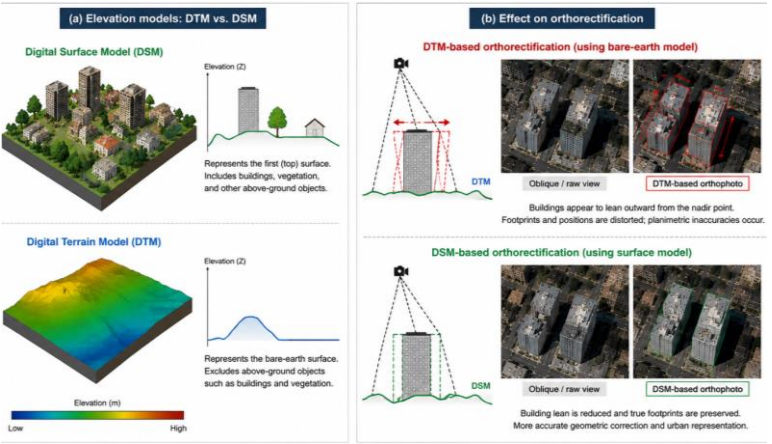
In addition to radial displacement, vertical structures frequently lead to occlusion, a condition in which buildings obstruct the visibility of ground features located behind them. Roads, pavements, utility infrastructure, and smaller buildings may become

partially or completely hidden in aerial photographs due to obstruction from taller structures (Qin et. al., 2015). This issue is especially common in narrow urban corridors, where adjacent buildings visually overlap and create blind spots in photogrammetric outputs. Moreover, shadows cast by tall buildings can reduce image contrast, making feature matching more difficult and often contributing to noisy or incomplete point cloud generation (Jiménez-Jiménez et. al., 2021).

**The Role of Elevation Models in Distortions Caused by High Vertical Structures**

The geometric accuracy of spatial products derived from aerial imagery is closely related to the quality and type of elevation model applied during orthorectification. In many conventional workflows, DTM are commonly used to represent bare-earth topography. However, because DTMs exclude above-ground elements, they cannot adequately account for buildings during geometric correction. Consequently, building façades are projected incorrectly onto the terrain surface, often resulting in positional inaccuracies and distortions in urban geometry (Trepekli et. al., 2022). By contrast, DSM include buildings, vegetation, and other above-ground features, providing a more realistic representation of vertical structures. As illustrated in Figure 7, DSM-based correction reduces building lean and improves the realism of urban modelling by incorporating actual elevation differences across the surface.

*Figure 7 Comparison between DTM- and DSM-based geometric correction*




*Trepekli et al. (2022) and Rau et al. (2002).*

In addition to model type, the spatial resolution of the elevation model plays an important role in correction quality. DSMs with low spatial resolution may oversimplify sharp building boundaries, which can lead to visual deformations such as edge smoothing, geometry erosion, and inaccuracies in roof delineation (Shen & Tan, 2020). For this reason, high-resolution elevation models are considered essential for reliable urban photogrammetric reconstruction.

## Possible Improvement Approaches for Distortions Caused by High Vertical Structures

Several approaches have been developed to reduce distortions associated with high vertical structures in aerial photogrammetry. Among these, the production of True Orthophotos is widely regarded as one of the most effective methods for minimizing building-related geometric errors. Unlike conventional orthophotos, which generally rely on DTM-based correction, true orthophotos are generated using DSM-supported orthorectification, allowing buildings to be positioned according to their actual footprint locations. By incorporating above-ground structures into the correction process, DSM-based approaches substantially reduce

building lean and improve positional consistency in urban mapping products (Rau et. al., 2002).

Another commonly adopted strategy is multi-view image acquisition, where multiple overlapping images are captured from different viewing directions. In dense urban areas, some features may remain hidden in a single image because of occlusion caused by adjacent buildings. However, objects obscured from one viewing angle often become visible in another perspective, improving scene completeness. Advanced photogrammetric algorithms combine these multiple observations to reconstruct hidden regions more reliably and enhance the geometric integrity of urban models (Stumpf et. al., 2014). This approach is particularly useful in environments characterized by narrow streets and closely spaced high-rise buildings, where visibility problems are more pronounced.

Beyond geometric correction methods, radiometric enhancement techniques also contribute to improving image quality and spatial interpretation. Methods such as local histogram equalization can increase contrast in shadowed regions, making features more distinguishable and facilitating feature extraction during photogrammetric processing (Łabędź et. al., 2021). Since shadows cast by tall structures frequently reduce image clarity in urban environments, radiometric improvements can help minimize information loss and support more stable image matching. When integrated within advanced photogrammetric workflows, these approaches collectively improve both positional accuracy and visual consistency, leading to more reliable spatial products in complex urban environments.

**Distortions Caused by Dense Vegetation and the Role of Elevation Models**

Dense vegetation represents a significant challenge in aerial photogrammetry because it limits the direct visibility of the ground

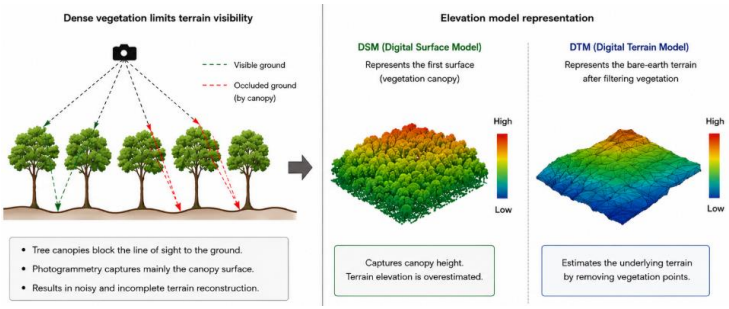
surface. Unlike active sensing technologies, photogrammetry operates as a passive sensing technique, meaning that surface reconstruction depends entirely on what is visible to the sensor. In forested and densely vegetated environments, tree canopies frequently obstruct the camera's line of sight, preventing accurate observation of the terrain beneath vegetation. As a result, elevation inaccuracies may occur during terrain reconstruction, particularly in areas where canopy density is high (Amhar et. al., 1998).

In addition to visibility limitations, vegetation introduces further complexity into photogrammetric processing because of its repetitive and dynamic surface characteristics. Since photogrammetric algorithms identify corresponding key points across overlapping images, similar textures formed by leaves and branches may produce ambiguous or incorrect matches. Wind-induced movement can further complicate image matching by introducing small positional differences between successive images. Consequently, vegetation-dense areas commonly exhibit noisy, fragmented, or blurred geometries in dense point clouds, reducing the reliability of terrain representation (Murtiyoso et. al., 2017).

The type of elevation model used plays a particularly important role in minimizing these inaccuracies. In many vegetation-covered areas, DSM primarily represent the upper canopy surface rather than the actual ground elevation. Therefore, terrain elevations derived only from photogrammetric point clouds may be overestimated by several meters, especially in densely forested regions (Amhar et. al., 1998). By contrast, DTM attempt to estimate the underlying bare-earth surface through vegetation filtering and interpolation procedures, thereby improving terrain representation beneath canopy cover. As illustrated in Figure 8, dense vegetation affects both terrain visibility and elevation modelling. While DSM products largely capture vegetation height and surface objects,

DTM-based representations seek to reconstruct the terrain beneath the canopy through classification and filtering processes.

*Figure 8 Effects of dense vegetation on terrain visibility and elevation model representation*




For this reason, reliable classification algorithms and interpolation methods are essential for separating vegetation from terrain points. In heavily vegetated environments, LiDAR-supported elevation models are often preferred because laser pulses can partially penetrate canopy gaps and provide more reliable terrain measurements. When integrated with photogrammetric workflows, these approaches substantially improve terrain modelling accuracy in vegetation-covered landscapes.

**Possible Improvement Approaches for Distortions Caused by Dense Vegetation**

Minimizing distortions in vegetation-dense environments requires improvements across both data acquisition and photogrammetric processing stages. Because dense canopy cover limits terrain visibility and introduces uncertainty into image matching, the quality of spatial products depends largely on how effectively vegetation-related limitations are addressed during workflow design.

One of the most widely adopted approaches involves increasing image overlap during flight planning. High forward and

side overlap ratios improve redundancy between consecutive images and increase the probability of identifying reliable matching features. In densely vegetated environments, where repetitive textures and canopy shadows frequently complicate key-point detection, forward overlap values exceeding 80–90% are often recommended to improve feature matching performance and reduce reconstruction gaps (Róg & Rzonca, 2021). Higher overlap also increases the number of viewing perspectives available for each surface element, helping to compensate for areas partially obscured by vegetation.

Another important consideration is the timing of image acquisition. Seasonal conditions can significantly influence terrain visibility in vegetated areas. Flights conducted during leaf-off periods, particularly in deciduous forest environments, generally provide improved visibility of the underlying terrain because reduced canopy density allows greater exposure of the ground surface (Amhar et. al., 1998). Under these conditions, photogrammetric algorithms can recover terrain characteristics more effectively, resulting in more reliable terrain modelling and improved DTM generation. In contrast, imagery acquired during periods of dense foliage often captures primarily canopy surfaces, increasing the likelihood of terrain overestimation.

Beyond acquisition strategies, advances in classification and filtering algorithms have contributed substantially to improving terrain reconstruction beneath vegetation. Point cloud filtering techniques are frequently applied to distinguish vegetation points from ground points based on elevation differences, slope relationships, and local geometric properties. Although filtering approaches can improve DTM accuracy, their performance may decline in areas characterized by extremely dense canopy cover or highly irregular terrain morphology.

For this reason, LiDAR-assisted workflows are increasingly preferred in vegetation-covered environments. Unlike passive photogrammetric methods, LiDAR systems actively emit laser pulses, some of which can penetrate canopy gaps and reach the underlying ground surface. This capability enables more reliable retrieval of terrain elevations beneath dense vegetation and often produces significantly more accurate bare-earth models than photogrammetry-only approaches (Varshosaz et. al., 2024). When LiDAR-derived elevation data are integrated with photogrammetric imagery, the resulting products generally exhibit higher geometric consistency and improved terrain representation.

In addition to geometric improvements, radiometric enhancement techniques can also contribute to more reliable image interpretation. Methods such as histogram equalization help improve contrast in shaded areas, making terrain-related features more distinguishable and facilitating feature extraction in low-visibility regions (Łabędź et. al., 2021). When combined with robust mosaicking and surface reconstruction workflows, these enhancements support the production of orthophoto products that are both visually consistent and geometrically more reliable.

Overall, reducing distortions in vegetation-dense environments requires a combination of careful flight planning, appropriate acquisition timing, reliable filtering strategies, and, where possible, integration with active sensing technologies. Rather than relying on a single solution, effective terrain reconstruction generally depends on combining complementary methods according to vegetation density and landscape complexity.

## Conclusions

The generation of accurate spatial products from aerial photographs depends not only on image quality but also on the effective management of geometric limitations associated with

photogrammetric acquisition and processing. Owing to its ability to rapidly capture large spatial areas at relatively low operational cost, aerial photogrammetry has become one of the most widely used approaches for producing orthophotos, digital elevation models, and three-dimensional spatial representations. Nevertheless, the geometric quality of these products remains strongly influenced by environmental conditions, terrain characteristics, acquisition geometry, and the suitability of the processing workflow.

This study focused primarily on two major sources of geometric distortion: high vertical structures and dense vegetation cover. In urban environments, tall buildings and other elevated structures introduce distortions related to radial displacement, building lean, occlusion, and shadow effects. Since aerial images are acquired through central perspective projection, vertically prominent objects are displaced away from the image center, leading to inaccuracies in building footprints and orthophoto production (Liu et. al., 2021; Dai et. al., 2011). Occlusion caused by closely spaced structures further limits ground visibility and may reduce the reliability of urban photogrammetric reconstruction, particularly in applications requiring high positional accuracy.

Dense vegetation presents a different but equally important challenge. In forested and vegetation-covered areas, photogrammetric reconstruction is often limited to canopy surfaces rather than the underlying terrain, creating systematic errors in terrain representation (Amhar et. al., 1998). In addition, repetitive vegetation textures and canopy movement may reduce feature matching performance, contributing to noisy point clouds and incomplete surface reconstruction (Murtiyoso et. al., 2017). These limitations make reliable terrain modelling particularly difficult in densely vegetated environments.

The findings also underline the importance of selecting an appropriate elevation model during orthorectification and terrain

reconstruction. While DTM are effective for representing bare-earth topography, they may not adequately capture discontinuities introduced by buildings and vegetation. DSM, on the other hand, include above-ground objects and therefore provide a more realistic representation of urban environments. However, the effectiveness of DSM-based correction depends considerably on model resolution and the geometric detail of the reconstructed surface (Trepekli et. al., 2022).

Several approaches were identified as effective in reducing geometric distortions in aerial-photograph-derived products. DSM-supported true orthophotos provide a reliable solution for minimizing building lean and positional inaccuracies in urban areas (Rau et. al., 2002). Similarly, multi-view image acquisition, increased image overlap, and radiometric enhancement techniques can improve reconstruction quality in areas affected by occlusion or shadowing (Łabędź et. al., 2021). In vegetation-dense environments, the integration of LiDAR technology offers important advantages because of its ability to retrieve terrain information beneath canopy cover more reliably than photogrammetry alone (Varshosaz et. al., 2024).

Overall, achieving geometrically reliable spatial products requires more than high-resolution aerial imagery. Accurate results depend on the integration of suitable flight planning, appropriate overlap strategies, robust elevation modelling, and processing methods adapted to local environmental conditions. Future research may further improve geometric reliability through the integration of artificial intelligence-based image enhancement, hybrid LiDAR–photogrammetry workflows, and automated error correction approaches, particularly in environments characterized by complex urban structures and dense vegetation.

## References

Amhar, F., Jansa, J., & Ries, C. (1998). The generation of true orthophotos using a 3D building model in conjunction with a conventional DTM. *International Archives of Photogrammetry and Remote Sensing, 32*(Part 4), 16-22. https://www.isprs.org/proceedings/XXXII/part4/jansa57.pdf

Arrighi, C., & Campo, L. (2019). Effects of digital terrain model uncertainties on high-resolution urban flood damage assessment. *Journal of Flood Risk Management, 12*(S2), e12530. https://doi.org/10.1111/jfr3.12530

Dai, F., Dong, S., & Lu, M. (2011). Photogrammetry assisted measurement of interstory drift for rapid post-disaster building damage reconnaissance. *Journal of Nondestructive Evaluation, 30*(3), 201-212. https://doi.org/10.1007/s10921-011-0108-6

Gonçalves, G., Gonçalves, D., Gómez-Gutiérrez, Á., Andriolo, U., & Pérez-Alvárez, J. A. (2021). 3D reconstruction of coastal cliffs from fixed-wing and multi-rotor UAS: Impact of SfM-MVS processing parameters, image redundancy and acquisition geometry. *Remote Sensing, 13*(6), 1222. https://doi.org/10.3390/rs13061222

Jiang, S., Jiang, W., & Wang, L. (2021). Unmanned aerial vehicle-based photogrammetric 3D mapping: A survey of techniques, applications, and challenges. *IEEE Geoscience and Remote Sensing Magazine, 10*(2), 135-171. https://doi.org/10.1109/MGRS.2021.3122248

Jiménez-Jiménez, S., Ojeda, W., Marcial, M. D., & Enciso, J. (2021). Digital terrain models generated with low-cost UAV photogrammetry: Methodology and accuracy. *ISPRS*

*International Journal of Geo-Information, 10*(5), 285. https://doi.org/10.3390/ijgi10050285

Łabędź, P., Skabek, K., Ozimek, P., & Nytko, M. (2021). Histogram adjustment of images for improving photogrammetric reconstruction. *Sensors, 21*(14), 4654. https://doi.org/10.3390/s21144654

Liu, J., Xu, W., Guo, B., Zhou, G., & Zhu, H. (2021). Accurate mapping method for UAV photogrammetry without ground control points in the map projection frame. *IEEE Transactions on Geoscience and Remote Sensing, 60*, 1-9. https://doi.org/10.1109/TGRS.2021.3052466

Morgan, B., Ford, A., & Smith, M. (2019). Standard methods for creating digital skeletal models using structure-from-motion photogrammetry. *American Journal of Physical Anthropology, 169*(1), 194-200. https://doi.org/10.1002/ajpa.23803

Murtiyoso, A., Koehl, M., Grussenmeyer, P., & Freville, T. (2017). Acquisition and processing protocols for UAV images: 3D modeling of historical buildings using photogrammetry. *ISPRS Annals of the Photogrammetry, Remote Sensing and Spatial Information Sciences, IV-2/W2*, 163-170. https://doi.org/10.5194/isprs-annals-IV-2-W2-163-2017

Qin, R., Huang, X., Gruen, A., & Schmitt, G. (2015). Object-based 3-D building change detection on multitemporal stereo images. *IEEE Journal of Selected Topics in Applied Earth Observations and Remote Sensing, 8*(5), 2125-2137. https://doi.org/10.1109/JSTARS.2015.2424275

Rau, J. Y., Chen, N. Y., & Chen, L. C. (2002). True orthophoto generation of built-up areas using multi-view images. *Photogrammetric Engineering and Remote Sensing, 68*(6),

581-588. https://www.asprs.org/wp-content/uploads/pers/2002journal/june/2002_jun_581-588.pdf

Róg, M., & Rzonca, A. (2021). The impact of photo overlap, the number of control points and the method of camera calibration on the accuracy of 3D model reconstruction. *Geomatics and Environmental Engineering, 15*(2), 67-87. https://doi.org/10.7494/geom.2021.15.2.67

Shen, J., & Tan, F. (2020). Effects of DEM resolution and resampling technique on building treatment for urban inundation modeling: A case study for the 2016 flooding of the HUST campus in Wuhan. *Natural Hazards, 104*(1), 927-957. https://doi.org/10.1007/s11069-020-04198-z

Stumpf, A., Malet, J. P., Allemand, P., Deseilligny, M., & Skupinski, G. (2014). Ground-based multi-view photogrammetry for the monitoring of landslide deformation and erosion. *Geomorphology, 231*, 218-234. https://doi.org/10.1016/j.geomorph.2014.10.039

Trepekli, K., Balstrøm, T., Friborg, T., Fog, B., Albert, A., Kofie, R., & Møller-Jensen, L. (2022). UAV-borne, LiDAR-based elevation modelling: A method for improving local-scale urban flood risk assessment. *Natural Hazards, 113*(2), 1183-1207. https://doi.org/10.1007/s11069-022-05308-9

Varshosaz, M., Sajadian, M., Pirasteh, S., & Moghimi, A. (2024). Automated two-step seamline detection for generating large-scale orthophoto mosaics from drone images. *Remote Sensing, 16*(5), 903. https://doi.org/10.3390/rs16050903

# BÖLÜM 2

# SPATİAL-STATİSTİCAL EVALUATİON OF EARTHQUAKE ACTİVİTİES İN TÜRKİYE

**RAMAZAN GÜNGÖR**[1]

## Introduction

With each passing day, anthropogenic impacts and human activities on nature are progressively intensifying, inevitably precipitating natural disasters such as soil erosion/landslides, floods, slope failures, and earthquakes (Orimoloye et al., 2021). Earthquakes exhibit a complex process that inflicts substantial damage on human life and results in incalculable losses compared to other types of natural hazards (Yin et al., 2019). Due to the inherent complexity of seismic activity, research concerning the temporal and spatial occurrence of earthquakes has yet to yield definitive conclusions (Zhang et al., 2022). The fact that the physical mechanisms governing earthquake genesis remain unresolved fosters a particular scientific interest in seismic phenomena. Given that earthquake development is a process spanning extended geological timescales, investigating them entails a challenging and multifaceted research endeavour (Zhang et al., 2021). Consequently,

[1]Öğr. Gör. Dr, Manisa Celal Bayar Üniversitesi, Mimarlık ve Şehir Planlama, Orcid: 0000-0002-6338-8554

earthquake research holds profound significance worldwide. Although a definitive spatial correlation regarding earthquake distribution has not yet been fully established, it is well-documented that they are closely associated with tectonic plate Dynamics (Yildiz, 2008). Plates emerging as a consequence of neotectonics events constitute actively seismogenic zones today (Burke et al., 1980). The mechanism governing the interaction between earthquakes and fault zones is conceptualized within the framework of the elastic rebound theory. According to this approach, elastic deformation that develops across both fault blocks prior to seismic events leads to the accumulation of potential (strain) energy within lithospheric rocks. When this accumulated energy exceeds the shear strength and yield threshold of the rock mass, a sudden rupture occurs. The instantaneous energy released during this rupture propagates outward in the form of seismic waves, generating ground shaking—namely, earthquakes.

Having been exposed to destructive earthquakes throughout its history, Türkiye features a geographic setting characterized by active and intense tectonic Dynamics (Bozkurt, 2001). Situated within the seismotectonic framework of the Alpine-Himalayan orogenic belt, the Anatolian Plate exhibits clear determining effects of Paleotethyan and Neotethyan oceanic remnants and tectonic traces associated with these systems in its geological evolution (Şengör & Yılmaz, 1983). Previous studies have demonstrated that the north-northeastward motion of the Arabian and African plates, coupled with the birectional seafloor spreading of the Mid-Atlantic Ridge, is closely associated with earthquakes occurring in Türkiye (Işık, 2022). In other words, the North Anatolian Fault (NAF) and East Anatolian Fault (EAF) systems, which constitute the primary seismic backbone of Türkiye, have been formed as a result of the convergence between the Arabian and Eurasian plates, forcing the Anatolian block to exhibit northwards extrusion movements

(Eyidoğan, 2007). The vast majority of earthquakes occurring in Türkiye, which features a remarkably high number of active fault lines, are of tectonic origin (Özdoğan, 1993). These seismic events predominantly occur along active faults situated at plate boundaries. Given its tectonic framework, the most intense and destructive earthquakes in Türkiye have historically manifested along the NAF, the EAF, and the horst-graben systems of Western Anatolia (Ketin, 1994). NAF, extending approximately 1,200 kilometers between Karlıova (Bingöl) and the Northern Aegean Sea, follows a trajectory generally parallel to the Black Sea coastline. It functions as a right-lateral strike-slip intracontinental transform fault, forming the tectonic boundary between the Eurasian and Anatolian plates (Barka, 1983). In the literature, the NAF is frequently compared to the San Andreas Fault in the United States in terms of its structural and kinematic characteristics (Ketin, 1976). Similarly, Barka (1983) pointed out in his research that certain segments of the NAF and EAF systems share common characteristic features. On the other hand, the West Anatolian extensional regime (spanning the Aegean Sea, Western Türkiye, and Greece) is among the tectonic domains undergoing the most rapid deformation and extension on a global scale (Seyitoğlu & Işık, 2015). As a consequence of these geodynamic processes, the Aegean graben system has attained an extensive distribution through horst-graben structures within the fractured and fragmented morphology of the region. Geological assessments indicate that the Aegean extensional regime has undergone approximately 50% north-south extension since its inception; this evidence clearly corroborates the high seismic activity and active tectonic nature of the Aegean Region (Burke et al., 1980).

From a spatial perspective, a high correlation exists between faults and earthquakes (Sezer, 2006). Although the focal zones of earthquakes are associated with fault systems, it is essential to

identify hazardous areas prone to such events within these regions and to implement risk mitigation measures (Poyraz & Kalafat, 2013). The majority of these studies fall within the scope of earth sciences, within which Geographic Information Systems (GIS) and spatial statistical methods integrated with GIS are frequently employed (Tağıl & Alevkayalı, 2013). GIS plays an instrumental role in the utilization, storage, updating, mapping, analysis, and reporting of large-scale datasets required by various disciplines engaging in earth sciences (Poyraz & Kalafat, 2013). Not restricted solely to map production, GIS is utilized across a myriad of disciplines thanks to its compatibility with software catering to diverse requirements. Through these systems and methods, it is feasible to determine the localized impacts of large-scale phenomena such as earthquakes across various locations (Zimeras, 2008). By utilizing all geographic location and attribute data related to earthquakes in statistical and mathematical analyses via GIS, it enables the presentation of results in visual formats (Pektezel, 2015).

When earthquake catalogs compiled for the classification and investigation of seismic activity across the Earth are examined, it is observed that major earthquakes cluster within specific temporal intervals (Kagan & Jackson, 1991). Many of these earthquakes are associated with faults ruptured on specific dates. In other words, the science of paleoseismology reveals that major earthquakes exhibit spatial and temporal clustering (Marco et al., 1996). Spatial statistical methods are employed to analyze, interpret, and report seismic data clustered in specific regions. In recent times, these methods have been frequently utilized in earthquake research alongside the proliferation of GIS technologies and the development of software adapted to statistical science.

Since the surface projection points (epicenters) of earthquakes are expressed by coordinate pairs, the spatial patterns of seismic activity can be examined based on these points. Such

analyses conducted using spatial statistical methods are of great importance in elucidating the relationship between earthquakes and faults (Mouslopoulou & Hristopulos, 2011). It is well-established that major earthquakes globally exhibit a tendency to cluster (Kagan & Jackson, 1991). Therefore, elucidating the spatial and temporal relationship between faults and earthquakes is of paramount importance for interpreting the data meaningfully.

The objective of this study is to elucidate the spatial patterns of the epicentral distributions of earthquakes with magnitudes of $M_w \geq 3.5$ that occurred in Türkiye between 1926 and 2026. In this context, the spatial distribution and clustering characteristics of seismic activities occurring within and surrounding Türkiye were investigated using GIS-based spatial analysis techniques.

**Study Area**

Türkiye, located in the middle latitudes of the Northern Hemisphere between $36° - 42°$ North parallels and $26° - 45°$ East meridians according to the geographic coordinate system, has been selected as the study area (Figure 1). Considering global seismic belts, Türkiye is under the influence of the Alpine-Himalayan seismic belt, one of the most active deformation zones in the world. The Anatolian Plate, upon which it resides, is bounded by the Eurasian Plate to the north, the African and Arabian plates to the south, the East Anatolian Compression Block to the east, and the Aegean Extensional Block to the west. This complex geodynamic setting places nearly the entire country under high-degree seismic hazard. In fact, citing data from the United States Geological Survey (USGS), Bikçe (2015) notes that a remarkable 6% of historical earthquakes recorded on a global scale have occurred within the borders of Türkiye.

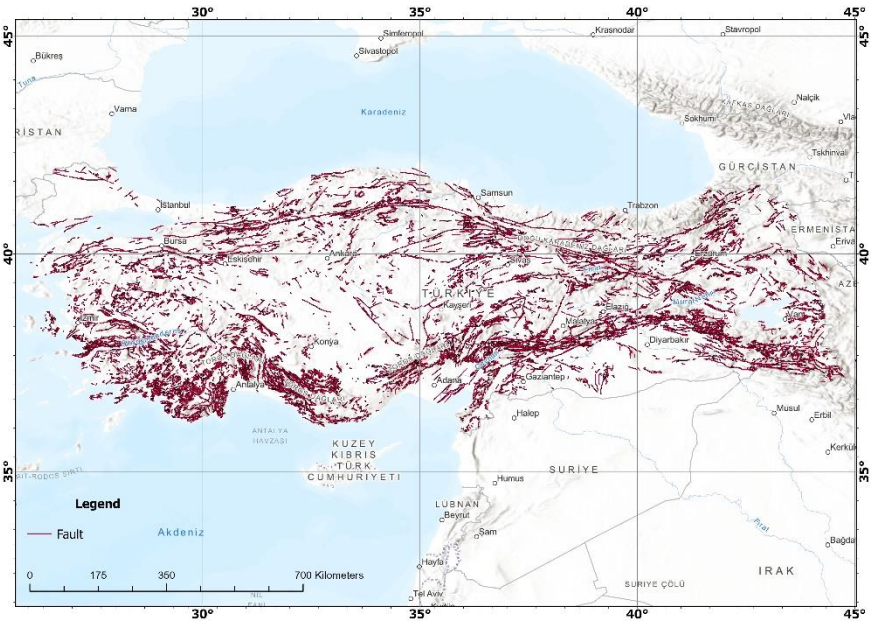



*Figure 1 Study area*

## Datasets

In this study, seismic data for 11,349 earthquakes with magnitudes of M$w \geq 3.5$, occurring at focal depths ranging from 0 to 200 km, were utilized for the period between 1926 and 2026. The data were obtained from the United States Geological Survey (USGS) earthquake catalog by applying spatial and temporal filters (https://earthquake.usgs.gov/earthquakes/search/). Each earthquake within the dataset was integrated into the ArcGIS Pro 3.2 GIS software based on its location coordinates; subsequent attribute data—including location, magnitude, date, time, and depth—were generated. The World Geodetic System 1984 (WGS84) was employed as the coordinate system throughout the study. Furthermore, fault data were obtained from the General Directorate of Mineral Research and Exploration (MTA) to analyze the spatial relationship between earthquake epicenters and active faults.

## Spatial Statistics

Variables observed on a geographical and spatial plane do not always satisfy the assumption of complete independence, as they are structurally interacting with one another. This situation increases the need for specialized analytical approaches capable of directly modeling spatial interactions and dependency structures among variables in the analysis of spatial datasets. In particular, the phenomenon of spatial autocorrelation—the fundamental characteristic of spatial data—makes it necessary for spatial statistics to diverge from traditional statistical methods and adopt a unique methodological framework. Although spatial statistics encompasses descriptive and inferential analysis dimensions just like classical statistics, it incorporates distinct techniques and formulations to address the complexity introduced by the spatial structure (Akyürek, 2019).

Spatial statistics is an analytical methodology rooted in probability theory, centering on the relationships and interactions between parametric values—such as distance, metric length, and area—and geographic location. Offering a comprehensive pool of techniques developed to characterize and model spatial data, this discipline enables the multidimensional examination of data-specific geographic models, distribution patterns, trends, and relationships. By allowing critical variables such as Euclidean or geographic distances, degrees of proximity, dispersion patterns, orientations, and spatial autocorrelation to be modeled with high sensitivity, spatial statistical methods are now widely utilized across many diverse scientific disciplines (Çubukçu, 2015).

The fundamental objective of spatial statistics is to identify spatial variations in attribute values within a dataset and to reveal the spatial pattern of these values (Erdoğan, 2010). In this context,

spatial variation is defined as a fundamental property used to detect clusters and concentrations formed by high or low values within a dataset. Following the identification of spatial variation, the next analytical step is to explain the dynamics driving these clusters or concentrations to exhibit high or low values in the studied areas. On the other hand, in certain advanced spatial analysis fields such as geostatistics, the primary objective is to perform spatial estimation and prediction of attribute values at un-sampled locations (Kasap & Gürlen, 2003)

**Global Moran's I Index**

To determine the degree of spatial autocorrelation among geographical points and their associated data within the study area, various test procedures accounting for different distance-based and sequential relationships have been developed in the literature. The most prominent among these approaches is Moran's spatial autocorrelation coefficient, introduced to the literature by Moran in 1950. Also referred to as the Global Moran's I Index (GMI), this statistical tool measures the intensity of spatial dependence by jointly considering the geographical coordinates of observations and their corresponding attribute values, thereby revealing the overall autocorrelation level and dispersion characteristics of the dataset (Akyürek & Arslan, 2018). The Moran's I statistical value is calculated as shown in Equation 1.

$$I=\frac{n}{S_0}\frac{\sum_{i=1}^{n}\sum_{j=1}^{n}w_{ij}(X_i-\bar{X})(X_j-\bar{X})}{\sum_{i=1}^{n}(X_i-\bar{X})^2} \quad (1)$$

Where, $x_i$, $i$ represents the variable value for location; $x_j$, $j$ represents the variable value for location; $\bar{X}$, denotes the arithmetic mean of the relevant variable; $w_{ij}$, $i$ ile $j$ s the spatial weight value defining the neighborhood and proximity relationship between points; $n$, represents the total number of points or features within the

scope of the analysis; and $S_0$, *t* denotes the sum of all spatial weights. The Moran's I index value determined by Equation 1

$$E(I)=\frac{-1}{n-1} \quad (2)$$

The obtained value is interpreted by comparing it with the theoretical expected index value calculated via the formula. The calculated *I* value being greater than the expected value $I > E(I)$, indicates that the point features in the dataset exhibit positive spatial autocorrelation—in other words, locations with similar attribute values are geographically close to each other and display a clustering tendency. Conversely, the condition *I<E(I)* demonstrates that there is no prominent clustering tendency and that the data follow a heterogeneous or uniform distribution across the spatial plane. Furthermore, the fulfilment of the condition *I≈E(I)* implies that the point data exhibit a random distribution and lack spatial dependence regarding the examined attribute. (Gayır & Arslan, 2022). The Global Moran's I statistic can take values ranging from -1 to +1; accordingly, +1 represents perfect positive spatial autocorrelation (strong clustering), -1 represents perfect negative spatial autocorrelation (regular/dispersed distribution), and a value around 0 represents spatial randomness (Affan et al., 2016).

**Getis-Ord G* Statistic**

*Getis-Ord G** statistic is used to determine whether there are spatial clustering tendencies of similar values at dataset points and to locate these spatial clusters. This method reveals the spatial areas where high values (hot spots) and low values (cold spots) are concentrated within the dataset. Depending on the magnitude of the statistically calculated *z-score*, the degree of clustering of high values (hot spots) increases proportionally. Conversely, the absolute increase of the *z-score* in the negative direction indicates the intensity of cold spot clustering formed by low values. If the calculated *G** value is close to zero, it can be stated that there is no

prominent high or low value clustering in the neighborhood of the respective feature, meaning that the spatial distribution is random (Akyürek & Arslan, 2018). The *Getis-Ord G** statistic is calculated as shown in Equation 3.

$$Gi^{*}=\frac{\sum_{j=1}^{n} w_{ij}X_j - \bar{X}\sum_{j=1}^{n} w_{ij}}{S\sqrt{\frac{[(n\sum_{j=1}^{n} w_{ij}^2)-(\sum_{j=1}^{n} w_{ij})^2]}{n-1}}} \quad (3)$$

Where $n$, represents the total number of points in the dataset; $x_j$, $j$ represents the variable value for location; $w_{ij}$, $i$ ile $j$ is the spatial weight coefficient defining the neighborhood and proximity relationship between points; $\bar{X}$ denotes the arithmetic mean of the relevant variable. The value of *S*, which serves as the basis for calculating the *Getis-Ord G** statistic, is computed using the relation presented in Equation 4.

$$S=\sqrt{\frac{[\sum_{j=1}^{n} x_j^2]}{n}-(X)^2} \quad (4)$$

**Anselin Local Moran's I Statistic**

While the Moran's I index reveals the average spatial dependency trend across the entire study area, it cannot precisely determine in which sub-regions of the study area local clusters or spatial anomalies occur. Developed to overcome this methodological limitation, the Anselin Local Moran's I analysis plays a critical role in identifying local-scale clusters formed by locations with similar or dissimilar attribute values, as well as spatial outliers. The highness of the index value calculated at the local level clearly demonstrates that values exhibiting similar characteristic features around the respective location (high-high or low-low structures) tend to cluster intensely on a local scale (Yakar, 2011). Conversely, a low or negative index value indicates that dissimilar values (high-low or low-high outliers) form a neighborhood relationship and that spatial

heterogeneity is dominant. Furthermore, the calculated *z-score* value provides information about the statistical significance and reliability of these obtained results. The Anselin Local Moran's I statistic is calculated as shown in Equation 5.

$$I_i = Z_i \sum_{j=}^{n} w_{ij} Z_j \quad (5)$$

Where $n$, represents the total number of points in the dataset; and $w_{ij}$ represents the spatial weight value defining the distance-based proximity and neighborhood relationships between locations $i$ and $j$.

The spatial weight matrix is a fundamental matrix structure that can be structured according to various neighborhood criteria, such as categorical or continuous distance, mathematically modeling the relative spatial relationships among all points in the study area. Accordingly, when examining the terms included in the matrix formulations, they represent the deviations of the variable values belonging to locations *i* and *j* from the arithmetic mean, respectively. For example, while the difference of the variable value from the mean for location $i$ is symbolized by a specific coefficient, this deviation value is calculated using the relation given in Equation 6.

$$Z_i = \frac{(X_i - \bar{X})}{\sigma} \quad (6)$$

The expression given here specifies the variable value for location *i*, the arithmetic mean value, and the standard deviation parameter belonging to the relevant variable, respectively. The standard deviation value, which provides a measure of dispersion for the distribution, is calculated via the formula given in Equation 7 (Akyürek & Arslan, 2018).

$$\sigma^2 = \frac{\sum_{i=1}^{n}(X_i - \bar{X})^2}{n-1} \quad (7)$$

## Results

The dataset within the scope of the study was classified chronologically into five distinct twenty-year periods: 1926–1946, 1946–1966, 1966–1986, 1986–2006, and 2006–2026. These classified periods were evaluated using various descriptive and spatial statistical methods based on the earthquake records that occurred within each period, and the obtained findings are presented in **Hata! Başvuru kaynağı bulunamadı.**.

All earthquakes between 1926 and 1946 occurred at magnitudes of $M_w$ 4.9, with the largest shock of this period being the 1939 Erzincan earthquake with a magnitude of 7.8 $M_w$; additionally, the Çankırı earthquakes with magnitudes of 7.6 $M_w$ and 7.5 $M_w$ occurred during this date range. In the 1946–1966 period, the highest magnitude was recorded as 7.3 $M_w$ during the earthquake centered in the Gönen district of Balıkesir. During the 1966–1986 period, earthquakes of 7.3 $M_w$ magnitude occurred in the provinces of Van, Sakarya, and Kütahya. Furthermore, the 1983 Erzurum-Narman earthquake with a magnitude of 6.8 $M_w$, the 1986 Adıyaman-Doğanşehir earthquake with a magnitude of 6.1 $M_w$, and the 1983 Çanakkale-Biga earthquake with a magnitude of 6.1 $M_w$ took place during this period. In the 1986–2006 period, the 7.6Mw Kocaeli-Gölcük and 7.3 $M_w$ Düzce earthquakes occurred. A large number of earthquakes were recorded nationwide during this period, with high values clustering in the provinces of Düzce, Erzincan, Afyonkarahisar, İzmir, Muğla, Kocaeli, Tunceli, and Amasya, while low values concentrated in the northwestern part of the country. In the 2006–2026 period, the most devastating shocks occurred in Kahramanmaraş on February 6, 2023, with two major earthquakes of 7.8 $M_w$ and 7.5 $M_w$ magnitudes striking successively on the same day.

*Table 1 Descriptive Statistics of Earthquakes*

| Period | Count | Percent (%) | Magnitude ($M_w$) | | | | Depth (Km) | |
|---|---|---|---|---|---|---|---|---|
| | | | Max | Min | Mean | Standard Deviation | Max | Min |
| 1926-1946 | 214 | 1.81 | 7.8 | 4.9 | 5.6 | 0.47 | 70 | 10 |
| 1946-1966 | 164 | 1.38 | 7.7 | 5.1 | 5.6 | 0.48 | 71.2 | 10 |
| 1966-1986 | 1661 | 14.02 | 7.3 | 3.5 | 4.3 | 0.62 | 180 | 2 |
| 1986-2006 | 5454 | 46.03 | 7.6 | 3.5 | 3.9 | 0.44 | 200 | 0 |
| 2006-2026 | 4355 | 36.76 | 7.8 | 3.5 | 4.3 | 0.45 | 176 | 0 |

The examination of Türkiye's seismicity data between 1926 and 2026 in twenty-year periods clearly reveals the change in earthquake record quality and catalog incompleteness parallel to the technological development of seismological observation networks. While the recording of less than approximately 3% of seismicity during the 1926–1966 period stemmed from the sparse observation network of the early instrumental era, a major surge in earthquake frequency occurred after 1966 with the increase in the number and sensitivity of stations; particularly in the 1986–2006 and 2006–2026 periods, more than 82% of total records were incorporated into the system. Over the century-long process, the stabilization of maximum magnitudes between 7.3 $M_w$ and 7.8 $M_w$ confirms that the tectonic compression regime of the Anatolian plate maintains its upper limit, whereas the drop in the lower threshold of mean magnitudes down to the 3.5 $M_w$ levels, stabilizing between 3.9 and 4.3 $M_w$ from 5.6, clearly supports the increase in the micro-earthquake capture capacity of modern networks and the seismogenic characteristic of shallow-to-intermediate depth (0-200 km) crustal deformations.

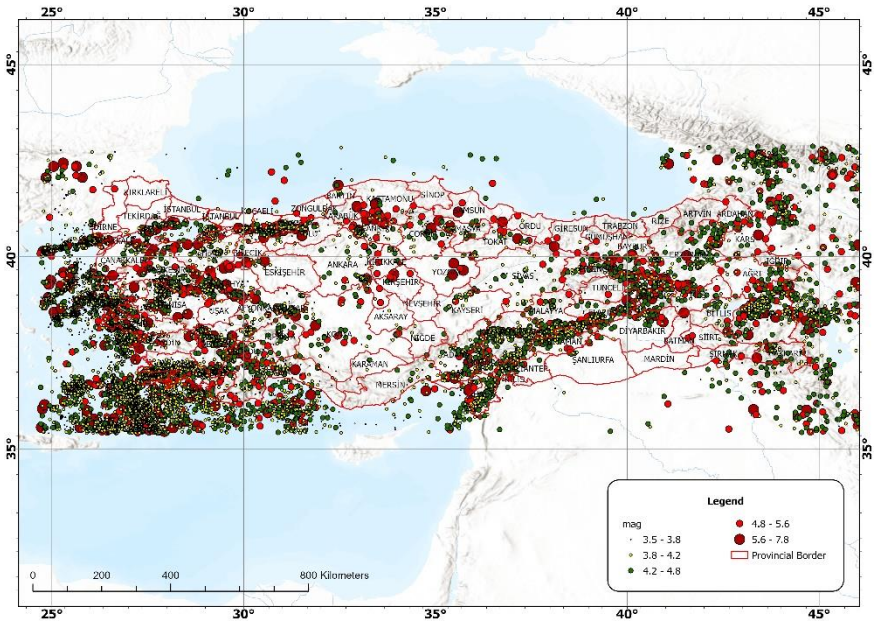



*Figure 2 Magnitude and Distribution of Earthquakes in Türkiye Between 1926 and 2026*

The Kernel Density analysis results revealed that earthquake events are not uniformly distributed across Türkiye and are concentrated along specific tectonic belts (Figure 2). The highest density values were determined in the southern part of the Aegean Sea and around Muğla, reflecting the effects of the Hellenic Subduction-Accretion Zone and the West Anatolian extensional regime. While the secondary density areas observed in and around İzmir are associated with the West Anatolian graben system, the increase in density detected around Lake Van demonstrates the active tectonic structure of Eastern Türkiye. The results demonstrate that earthquake activity is clustered along specific seismotectonic zones in Türkiye and that especially Western Anatolia and the Eastern Mediterranean are regions with high seismic activity.

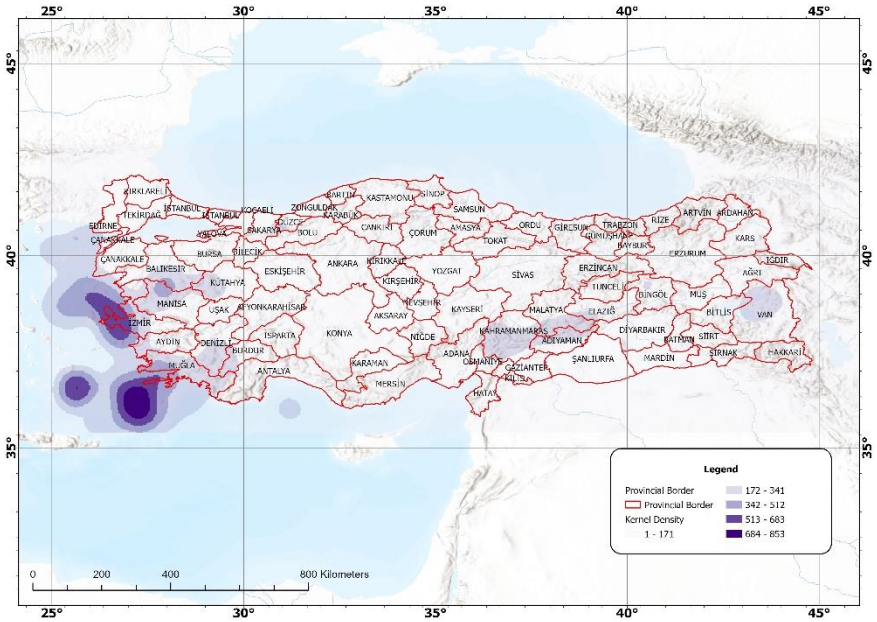



*Figure 3 1926-2026 Kernel Denstiy*

The results of the Average Nearest Neighbor (ANN) analysis applied to the 100-year seismicity dataset of Türkiye covering the period 1926–2026 demonstrate that seismic activity was not spatially random throughout any of the examined periods ($p < 0.001$). Rather, the results consistently indicate a statistically significant and pronounced clustering tendency, with Nearest Neighbor Ratios (NNR) ranging from 0.52 to 0.71 (Table 2). The substantial decline in the observed mean nearest-neighbor distance, from approximately 38.00 km during the early instrumental period to approximately 6.36 km in the modern period, can be primarily attributed to the increased technological capacity of seismological monitoring networks and the consequent densification of earthquake catalogues through enhanced detection sensitivity, particularly for microearthquakes. Nevertheless, the absolute *z-score* values, ranging from −8.16 to −60.82, further confirm the increasing statistical power associated

with the growing sample size. Spatially, these findings demonstrate that seismic energy has not been homogeneously distributed over the century; instead, earthquake occurrences have exhibited persistent clustering along major seismogenic structures, particularly the NAF, EAF, and the Western Anatolian neotectonic belt.

*Table 2 Average Nearest Neighbor Statistics*

| Period | Obs.Mea. Dist.(km) | Exp. Mean Distance | Nearest Neighbour Ratio | z-score | p-value | Correlation |
|---|---|---|---|---|---|---|
| 1926-1946 | 38.00 | 53.65 | 0,71 | -8,16 | 0.00 | Cluster |
| 1946-1966 | 37.55 | 61.20 | 0.62 | -9.47 | 0.00 | Cluster |
| 1966-1986 | 10.87 | 19.81 | 0.55 | -35.18 | 0.00 | Cluster |
| 1986-2006 | 6.49 | 10.98 | 0.59 | -57.75 | 0.00 | Cluster |
| 2006-2026 | 6.36 | 12.28 | 0.52 | -60.82 | 0.00 | Cluster |

The *Getis-Ord Gi** hot spot analysis was applied to identify the spatial clustering patterns of earthquake magnitude values recorded in the USGS Earthquake Catalog for the period 1926–2026 (Figure 4). The analysis evaluated the spatial clustering of high and low magnitude values within their respective neighbourhood relationships, with statistical significance classified at the 90%, 95%, and 99% confidence levels. Accordingly, areas with positive *Gi* z-scores* were interpreted as hot spots, representing clusters of relatively high magnitude values, whereas areas with negative *Gi* z-scores* were identified as cold spots, representing clusters of relatively low magnitude values.

The results demonstrate that earthquake magnitude values across Türkiye do not exhibit a spatially homogeneous distribution but instead show pronounced regional differentiation. In particular, high-magnitude earthquakes are strongly clustered in Eastern Anatolia, northeastern Türkiye, and the eastern sections of the North

Anatolian Fault Zone (NAFZ). Numerous observations within these regions were identified as hot spots at the 99% confidence level, with the clusters exhibiting the highest statistical significance represented by red areas on the map. Hot spots detected at the 95% and 90% confidence levels extend around these core clusters, indicating a broader spatial continuity in the distribution of high-magnitude earthquakes. A particularly prominent concentration of high-magnitude values is observed along the Erzincan–Bingöl–Muş–Bitlis–Van–Hakkâri corridor. Similarly, hot spot clusters at the 95% and 99% confidence levels were identified along the Bolu–Çankırı–Amasya–Tokat–Sivas–Erzincan segment of the North Anatolian Fault Zone. These findings indicate that high-magnitude earthquakes tend to cluster spatially along Türkiye's major active tectonic belts. In the south, statistically significant clusters of high-magnitude values are also evident around Hatay and the eastern Mediterranean region.

In contrast, Western Anatolia and the Aegean Sea, particularly along the İzmir–Aydın–Muğla corridor and across a substantial portion of the Aegean Sea, are characterized by pronounced clustering of low-magnitude values. In these areas, cold spots exhibit extensive spatial distributions at the 95% and, particularly, the 99% confidence levels. The identification of low-magnitude cold spots in the Aegean region, despite its high frequency of earthquake occurrence, demonstrates that the numerical density of earthquake events and the spatial distribution of their magnitude values do not necessarily exhibit the same spatial pattern. In other words, although numerous earthquakes occur in Western Anatolia, their magnitude values tend to be concentrated at lower levels compared with the high-magnitude clusters identified elsewhere in the study area.

In central Türkiye, hot and cold spot clusters are comparatively limited, and extensive areas do not exhibit

statistically significant spatial clustering. The predominance of the Not Significant class around Ankara, Konya, Aksaray, Nevşehir, Niğde, and surrounding areas indicates that neither high nor low magnitude values form pronounced spatial clusters within these neighbourhood structures.

The assessment of the *Getis-Ord Gi** results at three different confidence levels further demonstrates that the statistical strength of magnitude clustering varies spatially across Türkiye. Hot spots at the 99% confidence level represent the most robust spatial concentrations of high-magnitude values, whereas hot spots at the 95% and 90% confidence levels indicate clusters surrounding these core areas with comparatively lower levels of statistical significance. Likewise, the 99% confidence-level cold spots observed across Western Anatolia and the Aegean Sea indicate strong and spatially continuous clustering of relatively low-magnitude earthquake events.

When the *Getis-Ord Gi** results are evaluated in conjunction with the previously conducted Kernel Density analysis, an important distinction emerges. The Kernel Density analysis identified Western Anatolia and the Aegean Sea as areas characterized by high earthquake-event density, whereas the *Gi** analysis indicates that substantial portions of these same regions constitute cold spots with respect to earthquake magnitude. Conversely, in Eastern Anatolia, both high earthquake activity and high magnitude values are concentrated within statistically significant hot spots. Thus, when the two analytical approaches are considered jointly, a contrasting spatial pattern becomes evident: high earthquake frequency–low magnitude in western Türkiye and high earthquake frequency–high magnitude in eastern Türkiye.

These findings indicate that high-magnitude earthquakes are not randomly distributed across Türkiye's active fault systems but instead form statistically significant spatial clusters associated with

specific tectonic zones. Nevertheless, the *Getis-Ord Gi** results should not be interpreted as directly indicating the probability of a large earthquake occurring in a particular region in the future. Rather, the analysis identifies the statistically significant spatial clustering patterns characterizing the historical distribution of earthquake magnitude values recorded in the catalogue during the 1926–2026 period.

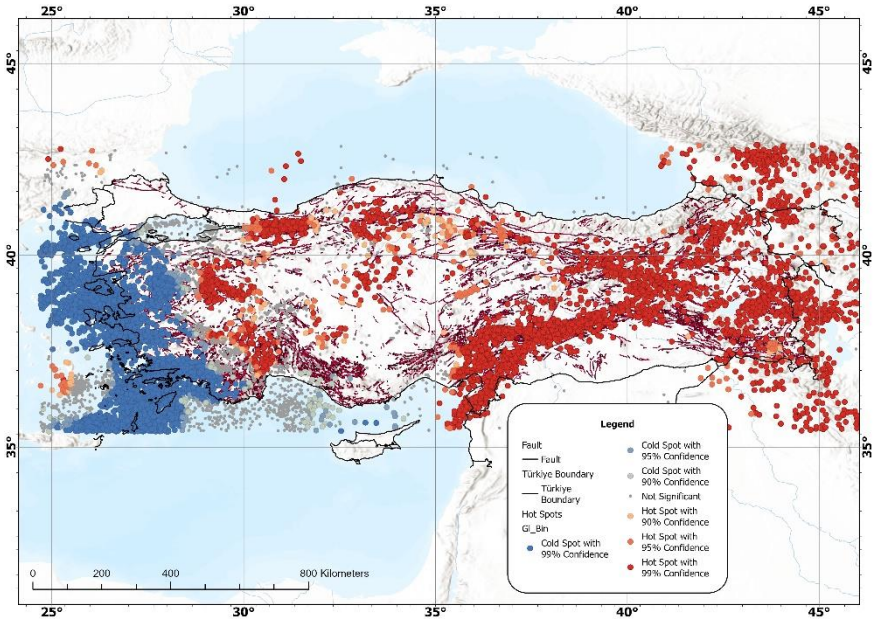



*Figure 4 Getis-Ord Gi* Hot and Cold Spot Clusters of Earthquake Magnitude Values, 1926–2026*

The results of the Global Moran's I spatial autocorrelation analysis applied to earthquake magnitude ($M_w$) data for Türkiye covering the period 1926–2026 demonstrate that the spatial distribution of seismic magnitudes is not random ($p < 0.001$) but instead exhibits statistically significant positive spatial autocorrelation ($I = 0.154$, $z = 81.00$). The positive Moran's I statistic confirms that earthquakes with similar magnitude values tend to occur in spatially proximate areas, forming statistically

significant clusters across the study region. The exceptionally high *z-score* of 81.00 provides compelling statistical evidence for the pronounced spatial dependence in the distribution of earthquake magnitudes, reflecting both the large sample size and the spatially structured nature of seismic energy accumulation along major seismogenic structures. These findings further indicate that the principal tectonic belts of Anatolia exert a substantial spatial control over the distribution and magnitude characteristics of seismic activity.

The Anselin Local Moran scatterplot is composed of four quadrants: the first quadrant (HH, "High–High"); the second quadrant (LH, "Low–High"); the third quadrant (LL, "Low–Low"); and the fourth quadrant (HL, "High–Low"). The first letter in each quadrant represents the value of the focal spatial unit, whereas the second denotes the corresponding value in its neighbouring spatial units (Cao et al., 2022). Values falling within the HH and LL quadrants represent spatially homogeneous associations characterized by strong positive spatial autocorrelation. In contrast, the LH and HL quadrants represent spatially heterogeneous associations characterized by strong negative spatial autocorrelation.

The Anselin Local Moran's I (LISA) analysis applied to the seismicity data of Türkiye for the 1926–2026 period reveals pronounced spatial heterogeneity and a distinct clustering typology among the country's different neotectonic regimes (Figure 5). Across the study area, High–High (HH) clusters exhibit a predominantly linear spatial continuity along major seismogenic structures, particularly the NAFZ and the East Anatolian Fault Zone (EAFZ), indicating strong spatial dependence in the distribution of high-magnitude seismic activity and highlighting the major role of these tectonic corridors in earthquake generation. In contrast, High–Low (HL) spatial outliers are predominantly concentrated within the extensional neotectonic regime of Western Anatolia, particularly the

Aegean region. Their occurrence within a widespread matrix of relatively frequent but generally low-magnitude microseismicity indicates the presence of isolated high-energy earthquake sources associated with major normal-fault systems, potentially reflecting localized asperities and the complex intracrustal deformation regime characteristic of Western Anatolia.

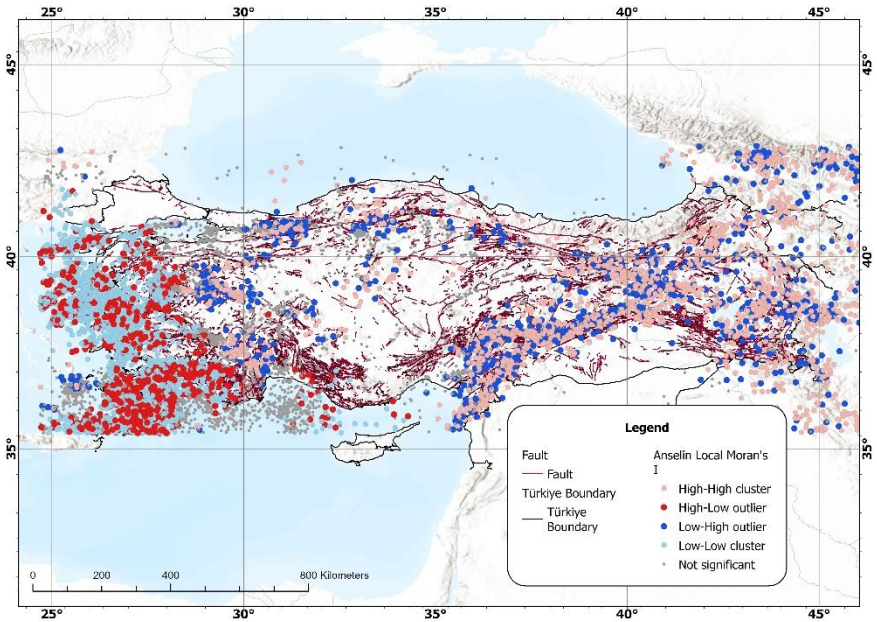



*Figure 5 Anselin Local Moran's I Clusters of Earthquake Magnitude, 1926–2026*

## Conclusion

The present study aimed to investigate the spatial distribution and clustering patterns of earthquakes that have occurred across Türkiye over the historical period. Within a GIS-based analytical framework, earthquakes with magnitudes of $M_w \geq 3.5$ recorded between 1926 and 2026 were examined using both global and local spatial statistical methods. Across all spatial statistical approaches employed, earthquake occurrences consistently exhibited significant

clustering tendencies and spatially interrelated patterns. When the earthquake catalogue was evaluated over different temporal periods, areas characterized by high-value clustering were generally concentrated around the locations of major earthquakes that occurred within the corresponding time intervals. The ANN analysis demonstrated that earthquake occurrences exhibit a persistent linear clustering pattern along the NAFZ, EAFZ, and the Western Anatolian neotectonic belt. Moreover, the reduction in observed mean nearest-neighbour distances from the relatively large values recorded during the early instrumental period to approximately 6 km in the modern period clearly reflects the enhanced capability of contemporary seismological networks to detect and catalogue smaller-magnitude seismic events.

A review of the existing literature reveals a relative scarcity of GIS-based studies focusing on earthquake management and seismic risk assessment. However, GIS and GIS-integrated spatial statistical techniques offer substantial potential for applications in disaster management, risk identification and assessment, earthquake susceptibility mapping, the identification and management of high-risk settlement areas, and the management of secondary hazards associated with earthquakes, including floods, landslides, and tsunamis. This is particularly important for Türkiye, which is situated within one of the world's seismically active regions and is characterized by several major active fault systems. Therefore, the systematic integration of GIS-based spatial analyses into earthquake risk management and disaster planning should be expanded at national and regional scales. Such approaches can provide a scientific basis for more effective land-use planning and risk-informed spatial management, thereby contributing to the reduction of potential economic losses, infrastructure damage, and human casualties associated with future earthquakes.

## References

Affan, M., Syukri, M., Wahyuna, L., & Sofyan, H. (2016). Spatial statistic analysis of earthquakes in Aceh Province year 1921–2014: Cluster seismicity. *Aceh International Journal of Science and Technology, 5*(2), 54–62. https://doi.org/10.13170/aijst.5.2.4878

Akyürek, Ö. (2019). *Uzaktan algılama görüntülerinde geoistatiksel yöntemler ile doku analizi* [Texture analysis in remote sensing images using geostatistical methods] [Master's thesis, Kocaeli University].

Akyürek, Ö., & Arslan, O. (2018). Kocaeli ili ve çevresinde (1900–2016) yılları arasında gerçekleşen tarihsel depremlerin konumsal istatistik analizi [Spatial statistical analysis of historical earthquakes occurring in Kocaeli Province and its surroundings between 1900 and 2016]. *Geomatik, 3*(1), 48–62. https://doi.org/10.29128/geomatik.333104

Barka, A. (1983). Büyük magnitüdlü depremlerin episantr alanlarını önceden belirleyebilecek bazı jeolojik veriler [Geological criteria for the forecasting of epicentral areas of large magnitude earthquakes]. *Türkiye Jeoloji Kurumu Bülteni, 26*, 21–30.

Bikçe, M. (2015). Türkiye'de hasara ve can kaybına neden olan deprem listesi (1900–2014) [List of earthquakes causing damage and loss of life in Türkiye (1900–2014)]. In *3. Türkiye Deprem Mühendisliği ve Sismoloji Konferansı* [3rd Turkish Earthquake Engineering and Seismology Conference] (pp. 14–16).

Bozkurt, E. (2001). Neotectonics of Türkiye—A synthesis. *Geodinamica Acta, 14*(1–3), 3–30. https://doi.org/10.1016/S0985-3111(01)01066-X

Burke, K., Grippi, J., & Şengör, A. M. C. (1980). Neogene structures in Jamaica and the tectonic style of the northern Caribbean plate boundary zone. *The Journal of Geology, 88*(4), 375–386.

Cao, Z., Zhang, H., Liu, Y., Liu, S., Feng, L., Yin, L., & Zheng, W. (2022). Spatial distribution analysis of seismic activity based on GMI, LMI, and LISA in China. *Open Geosciences, 14*(1), 89–97. https://doi.org/10.1515/geo-2020-0332

Çubukçu, K. M. (2015). *Planlamada ve coğrafyada temel istatistik ve mekânsal istatistik* [Basic statistics and spatial statistics in planning and geography]. Nobel Akademik Yayıncılık.

Erdoğan, S. (2010). Epidemiyolojide CBS uygulamaları: Konumsal kümeleme yöntemlerinin karşılaştırılması—Menenjit örneği [GIS applications in epidemiology: A comparison of spatial clustering methods—The case of meningitis]. *Harita Teknolojileri Elektronik Dergisi, 2*(2), 23–31.

Eyidoğan, H. (2007). Marmara Bölgesi'nin ve İstanbul kentinin deprem tehlikesi üzerine bir derleme [A review of the earthquake hazard of the Marmara Region and Istanbul]. In *TMMOB Afet Sempozyumu Bildiri Kitabı* [Proceedings of the TMMOB Disaster Symposium] (pp. 15–29). Mattek Matbaacılık.

Gayır, B., & Arslan, O. (2018). Orman yangınlarının CBS tabanlı konumsal istatistik analizi: 2011–2015 yılları arasında Muğla Orman Bölge sınırları içerisinde çıkan yangınlar [GIS-based spatial statistical analysis of forest fires: Forest fires occurring within the boundaries of Muğla Regional Directorate of Forestry between 2011 and 2015]. *Anadolu Orman Araştırmaları Dergisi, 4*(1), 46–62.

Işık, E. (2022). Comparative investigation of seismic and structural parameters of earthquakes (M ≥ 6) after 1900 in Türkiye. *Arabian Journal of Geosciences, 15*(10), 971. https://doi.org/10.1007/s12517-022-10255-7

Kagan, Y. Y., & Jackson, D. D. (1991). Seismic gap hypothesis: Ten years after. *Journal of Geophysical Research: Solid Earth, 96*(B13), 21,419–21,431. https://doi.org/10.1029/91JB02210

Kasap, R., & Gürlen, Ü. (2003). Deprem magnitüdleri için tekrarlanma yıllarının elde edilmesi: Marmara Bölgesi örneği [Obtaining the return periods of earthquake magnitudes: The case of the Marmara Region]. *Doğuş Üniversitesi Dergisi, 4*(2), 157–166.

Ketin, İ. (1976). San Andreas ve Kuzey Anadolu fayları arasında bir karşılaştırma [A comparison between the San Andreas and North Anatolian faults]. *Türkiye Jeoloji Kurumu Bülteni, 19*(2), 149–154.

Ketin, İ. (1994). *Genel jeoloji: Yerbilimlerine giriş* [General geology: An introduction to earth sciences]. İTÜ Vakfı Yayınları.

Marco, S., Stein, M., Agnon, A., & Ron, H. (1996). Long-term earthquake clustering: A 50,000-year paleoseismic record in the Dead Sea Graben. *Journal of Geophysical Research: Solid Earth, 101*(B3), 6,179–6,191. https://doi.org/10.1029/95JB01587

Mouslopoulou, V., & Hristopulos, D. T. (2011). Patterns of tectonic fault interactions captured through geostatistical analysis of microearthquakes. *Journal of Geophysical Research: Solid Earth, 116*(B7), B07305. https://doi.org/10.1029/2010JB007804

Orimoloye, I. R., Belle, J. A., & Ololade, O. O. (2021). Exploring the emerging evolution trends of disaster risk reduction research: A global scenario. *International Journal of Environmental Science and Technology, 18*(3), 673–690.

Özdoğan, S. (1993). Türkiye'nin deprem bölgeleri [Earthquake regions of Türkiye]. *Türkiye Coğrafyası Araştırma ve Uygulama Merkezi Dergisi, 2*, 53–68.

Pektezel, H. (2015). Coğrafi bilgi sistemleri (CBS) ve analitik hiyerarşi sistemine (AHS) göre Gelibolu Yarımadası'nın deprem duyarlılık analizi [Earthquake susceptibility analysis of the Gallipoli Peninsula using geographic information systems (GIS) and the analytical hierarchy process (AHP)]. *International Journal of Social Science, 36*, 179–201.

Poyraz, S. A., & Kalafat, D. (2013). Sismoloji'de CBS uygulamaları [GIS applications in seismology]. *Jeofizik, 18*, 47–58.

Seyitoğlu, G., & Işık, V. (2015). Batı Anadolu'da Geç Senozoyik genişleme tektoniği: Menderes çekirdek kompleksinin yüzeylemesi ve ilişkili havza oluşumu [Late Cenozoic extensional tectonics in western Anatolia: Exhumation of the Menderes core complex and associated basin formation]. *Maden Tetkik ve Arama Dergisi, 151*, 49–109.

Sezer, L. İ. (2006). Kaz Dağı yöresinde deprem aktivitesi ve riski [Earthquake activity and risk in the Kazdağı region]. *Ege Coğrafya Dergisi, 15*(1–2), 17–29.

Şengör, A. M. C., & Yılmaz, Y. (1983). Türkiye'de Tetis'in evrimi: Levha tektoniği açısından bir yaklaşım [The evolution of the Tethys in Türkiye: A plate tectonic approach]. *Türkiye Jeoloji Kurumu Yerbilimleri Özel Dizisi, 1*, 75–86.

Tağıl, Ş., & Alevkayalı, Ç. (2013). Ege Bölgesi'nde depremlerin mekânsal dağılımı: Jeoistatistiksel yaklaşım [Spatial distribution of earthquakes in the Aegean Region: A geostatistical approach]. *Uluslararası Sosyal Araştırmalar Dergisi, 6*(28).

Yıldız, N. (2008). *Kırşehir ilinin depremselliği* [Seismicity of Kırşehir Province] [Master's thesis].

Yin, L., Li, X., Zheng, W., Yin, Z., Song, L., Ge, L., & Zeng, Q. (2019). Fractal dimension analysis for seismicity spatial and temporal distribution in the circum-Pacific seismic belt. *Journal of Earth System Science, 128*, 22. https://doi.org/10.1007/s12040-018-1040-2

Zimeras, S. (2008). Exploratory point pattern analysis for modeling earthquake data. In *1st WSEAS International Conference on Environmental and Geological Science and Engineering (EG'08)*, Malta, September 11–13, 2008.

# BÖLÜM 3

# DETERMINATION OF SUITABLE AREAS FOR RAINWATER HARVESTING AND DROUGHT ANALYSIS IN DEMIRCI DISTRICT

**RAMAZAN GÜNGÖR**[1]

## Introduction

The pressure on water resources is steadily increasing under the influence of global climate change, posing a serious threat to water security, particularly in regions characterized by semi-arid climatic conditions (Arnell et al., 2011). A substantial proportion of the global population is directly affected by water scarcity due to both inadequate precipitation regimes and the unsustainable exploitation of groundwater resources (Alotaibi et al., 2023). Türkiye is also among the countries with a high risk of drought and frequently faces water scarcity resulting from irregular and insufficient seasonal precipitation (Özben & Güngör, 2024). This situation is rendering the country's existing water resources increasingly vulnerable. Such pressures necessitate the development of environmentally friendly and technology-assisted alternative solutions alongside conventional water supply methods. As one such

[1] Öğr. Gör. Dr, Manisa Celal Bayar Üniversitesi, Mimarlık ve Şehir Planlama, Orcid: 0000-0002-6338-8554

alternative, Rainwater Harvesting (RWH) has attracted considerable attention due to its low-cost and sustainable characteristics, contributing both to the replenishment of groundwater reserves and to meeting agricultural and domestic water demands (Hassan et al., 2025).

A substantial proportion of water consumption in Türkiye (73%) is associated with agricultural activities, making the widespread adoption of RWH practices strategically important for the conservation of potable water resources (Muratoglu, 2020). In addition, RWH can enhance soil moisture retention, reduce the risks of flooding and erosion, and contribute positively to agricultural productivity. However, the successful implementation of RWH requires the integrated assessment of multiple environmental and spatial variables. In this context, the combined use of Geographic Information Systems (GIS) and Multi-Criteria Decision-Making (MCDM) methods provides a scientific basis for the decision-making process and plays a critical role in identifying the most suitable areas for RWH implementation (Vohland & Barry, 2009).

The aim of this study is to identify the most suitable areas for RWH in Demirci District, Manisa Province, Türkiye. To this end, the Analytical Hierarchy Process (AHP), one of the widely used MCDM methods, was employed, and eight parameters frequently considered in the literature were integrated and analyzed within a GIS environment. The identified optimal areas were further compared with spectral indices used for drought monitoring, thereby enabling an assessment of the relationship between areas with high RWH potential and drought conditions.

**Study area**

Demirci, the study area, is a district located in Manisa Province within the Aegean Region of Türkiye. The northern and northeastern parts of the district are surrounded by the Demirci-

Simav Mountains (https://www.demirci-bld.gov.tr/). An examination of the Hydrologic Soil Groups (HSGs) in the region indicates that Groups B, C, and D are predominant. In particular, Groups C and D, which are considered suitable for RWH applications, account for approximately 88% of the study area (Radwan & Alazba, 2023). An analysis of precipitation records from the past four decades indicates that the mean annual precipitation ranges between 593 and 807 mm. This precipitation regime positively contributes to the maximum surface infiltration capacity, which is one of the key parameters influencing RWH suitability (Ammar et al., 2016). Considering these characteristics, Demirci District was selected as the study area for identifying suitable areas for RWH (Figure 1).

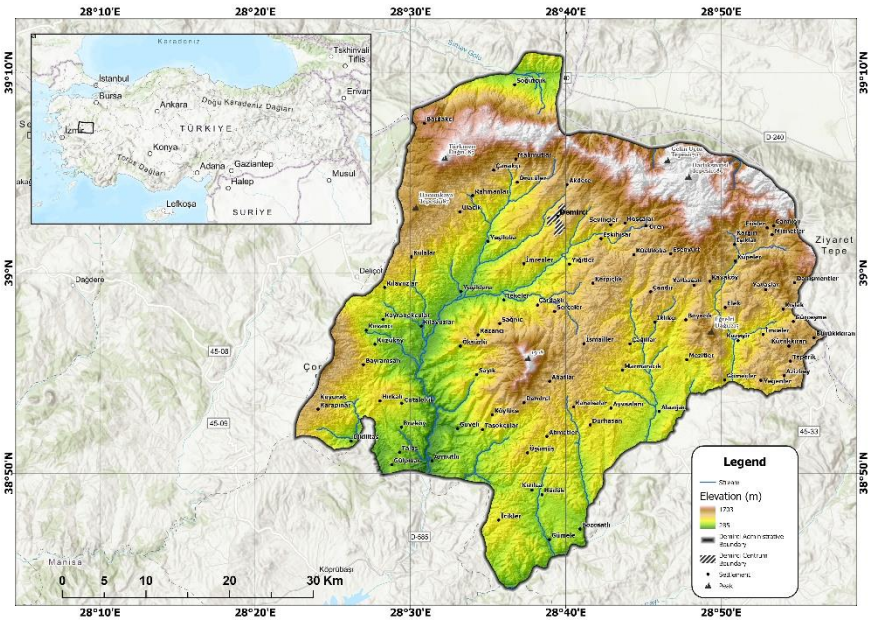



*Figure 1 Study area*

## Method

The research process consisted of four main stages (Figure 2). In the first stage, threshold values were established for the parameters commonly used in the literature for identifying suitable areas for RWH (Table 1). Subsequently, each data layer was divided into five classes and reclassified according to its characteristics. In the second stage, the Analytical Hierarchy Process (AHP) was applied to calculate the relative weights of the parameters. In the third stage, the layer maps generated using the calculated weights were overlaid to identify the areas most suitable for RWH. In the final stage, the identified suitable areas were compared with drought monitoring indicators, including the Temperature Condition Index (TCI) and Vegetation Health Index (VHI), derived from Moderate Resolution Imaging Spectroradiometer (MODIS) data for the 2010–2024 period (Table 2).

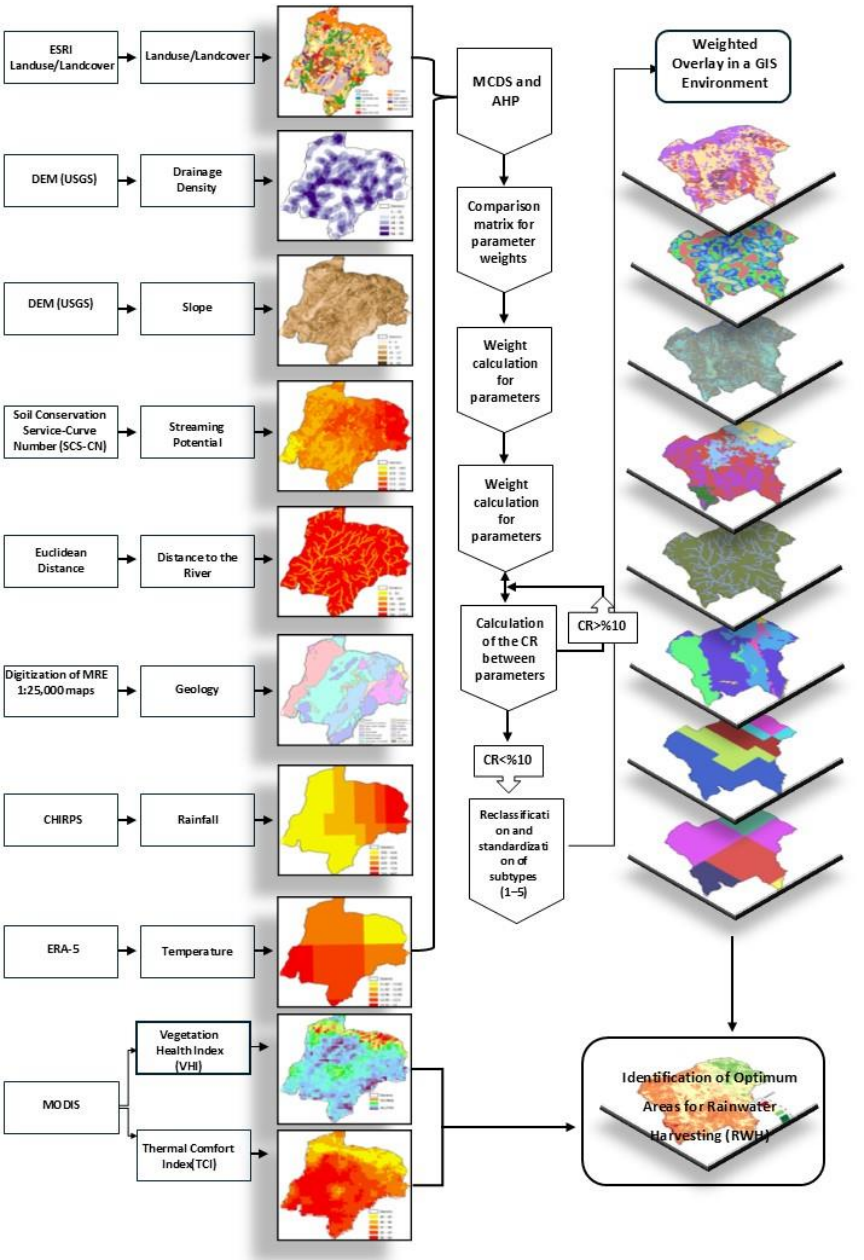



*Figure 2 Workflow diagram*

*Table 1 Parameters used in the study*

| Parameters | Data source / Method |
|---|---|
| Land Use/Land Cover (LULC) | ESRI Land Cover (livingatlas.arcgis.com/landcover) |
| Drainage Density | DEM (USGS), UTM-35, WGS 1984 (earthexplorer.usgs.gov) |
| Slope | DEM (USGS), UTM-35, WGS 1984 (earthexplorer.usgs.gov) |
| Flow Potential | Derived using the Soil Conservation Service–Curve Number (SCS-CN) method |
| Distance to Streams | Derived using the Euclidean Distance tool in ArcGIS Pro 3.1 |
| Geology | Digitization of MTA 1:25,000-scale maps using ArcGIS Pro 3.1 (yerbilimleri.mta.gov.tr) |
| Rainfall | CHIRPS: Rainfall Estimates from Rain Gauge and Satellite Observations (data.chc.ucsb.edu) |
| Temperature | ERA5-Land Monthly Aggregated (cds.climate.copernicus.eu) |

## Analytical Hierarchy Process (AHP)

The Analytical Hierarchy Process (AHP) is a Multi-Criteria Decision-Making (MCDM) technique developed by Saaty (1977) to determine the relative importance of different map layers and to evaluate their characteristics in an integrated manner. In this study, AHP was employed to assign weights to the parameters influencing the identification of suitable areas for RWH and to classify these parameters into appropriate subcategories.

## Spectral Drought Indices

*Table 2 Drought indices*

| Formula | No | Reference |
|---|---|---|
| $TCI = 100 \times (T_{max} - T_{observed}) / (T_{max} - T_{min})$ | (1) | (Kogan, 1995) |
| $VHI = \alpha \times VCI + (1 - \alpha) \times TCI$ | (2) | (Bento et al., 2018) |

Tmax: Maximum land surface temperature observed over the study area; T observed: Observed land surface temperature for the corresponding pixel; Tmin: Minimum land surface temperature observed over the study area; VCI: Vegetation Condition Index, which represents the health status of vegetation based on the Normalized Difference Vegetation Index (NDVI); α (alpha coefficient): Set to 0.5 in this study.

## SCS-CN Method

The Soil Conservation Service–Curve Number (SCS-CN) method is one of the most widely used approaches for estimating surface runoff resulting from precipitation events across different land cover classes (Equation 3). The method determines the Curve Number (CN) based on the characteristics of the HSGs (Equation 4) (Mishra & Singh, 2013).

$$Q = (P - 0{,}2S)^2 / (P + 0{,}8S) \quad [P < 0{,}2S \text{ ise } Q = 0] \tag{3}$$

$$S = 25400 / CN - 254 \tag{4}$$

where P is the total precipitation (mm), S is the maximum potential soil retention (mm), and Q is the runoff potential (mm). The CN value is determined based on the HSG and land cover characteristics.

## Results

Within the scope of the study, suitable areas for RWH were identified using the AHP method based on topographic and meteorological parameters. The pairwise comparison of the parameters revealed that the highest weight (27%) was assigned to the runoff potential parameter (Table 3). The consistency ratio (CR), calculated based on the consistency index and random index, was found to be 9%. Since this value is below the 10% threshold, the pairwise comparisons were considered to have an acceptable level of consistency. The maps of the selected parameters were reclassified into different class intervals and prepared for the overlay analysis (Figure 3).

*Table 3 Parameters and their weights*

| Criteria | Weight (%) |
|---|---|
| Land Use/Land Cover (LULC) | 10 |
| Drainage Density | 11 |
| Slope | 16 |
| Flow Potential | 27 |
| Distance to Streams | 6 |
| Geology | 5 |
| Rainfall | 22 |
| Temperature | 3 |

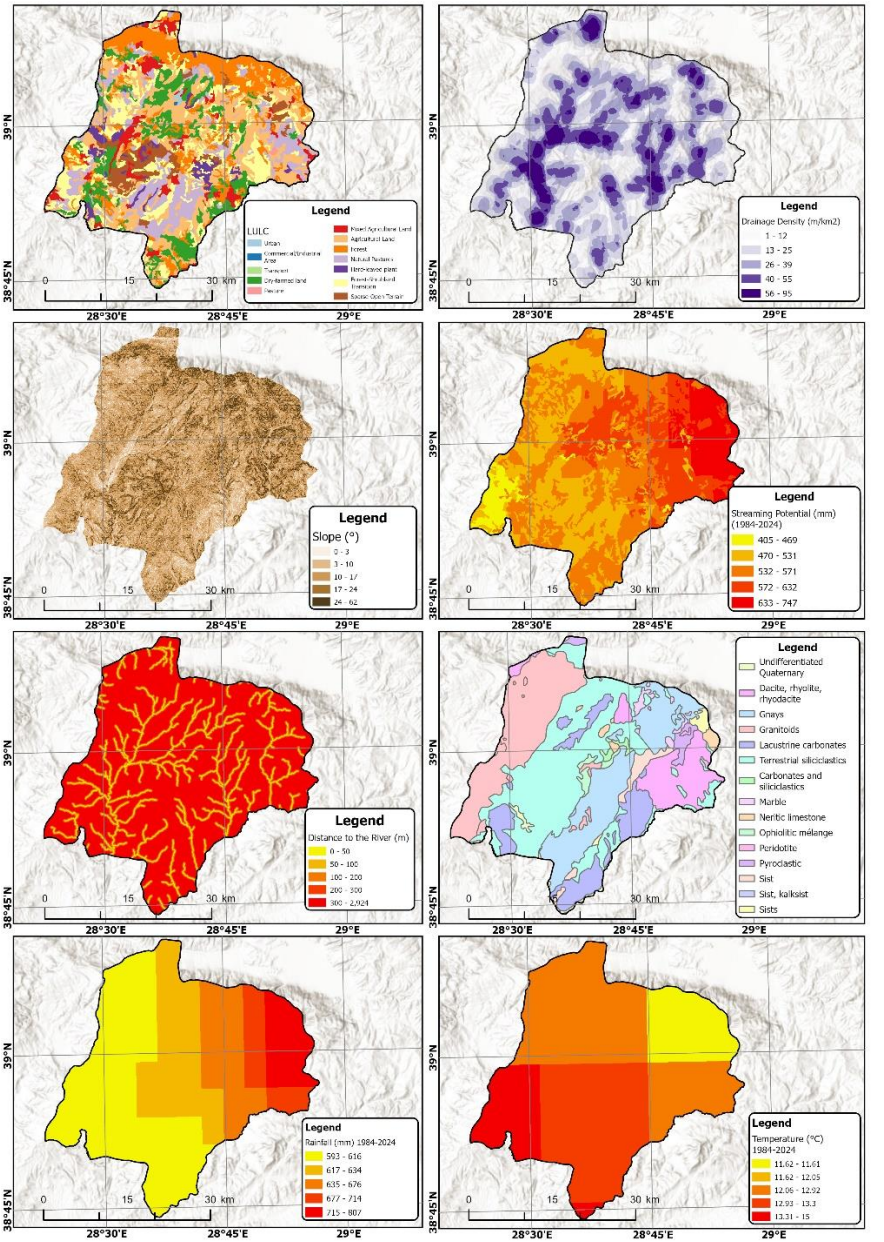



*Figure 3 Maps of the parameters used in the study*

The study area contains areas belonging to HSGs B, C, and D (Figure 4). The overlay of these groups with the land use/land cover (LULC) data revealed that the resulting CN values ranged from 55 to 95. The S values calculated from the HSG and CN data ranged from 13 to 208 mm, while the Q values ranged from 405 to 747 mm. These results indicate that the entire study area has a certain degree of runoff potential. In terms of RWH suitability, 693.25 km² (52.74%) of the study area was classified as suitable, whereas 621.26 km² (47.26%) was classified as unsuitable (Table 4). The identified suitable areas were predominantly concentrated in the northeastern part of Demirci District (Figure 5), with the largest proportion of these areas (250.92 km²) occurring on agricultural land.

*Table 4 RWH suitability classes*

| Class | Area (km²) | Ratio (%) |
|---|---|---|
| Not Suitable | 17.08 | 1.30 |
| Unsuitable | 604.18 | 45.96 |
| Moderately Suitable | 568.96 | 43.28 |
| Suitable | 123.52 | 9.40 |
| Highly Suitable | 0.77 | 0.06 |

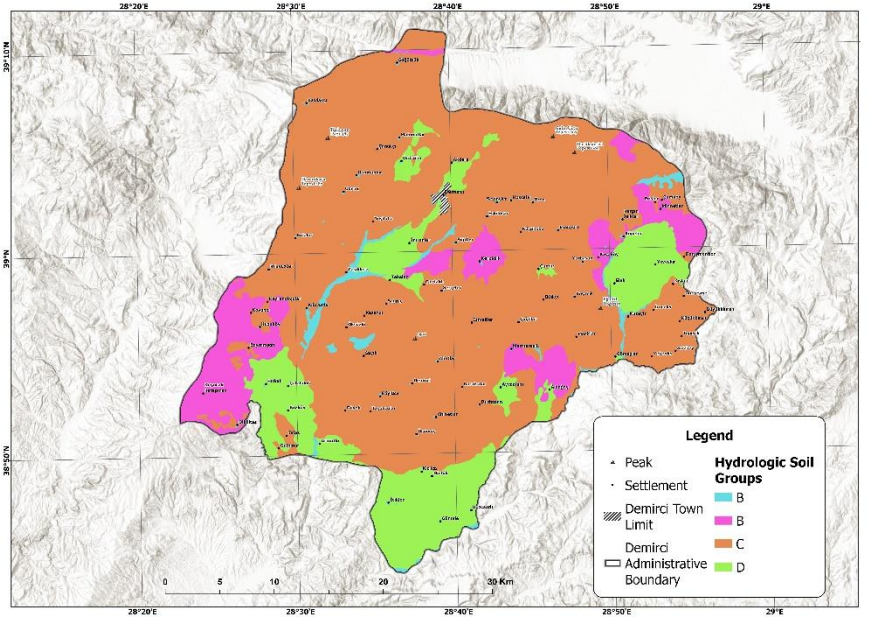



*Figure 4 Hydrologic Soil Groups*

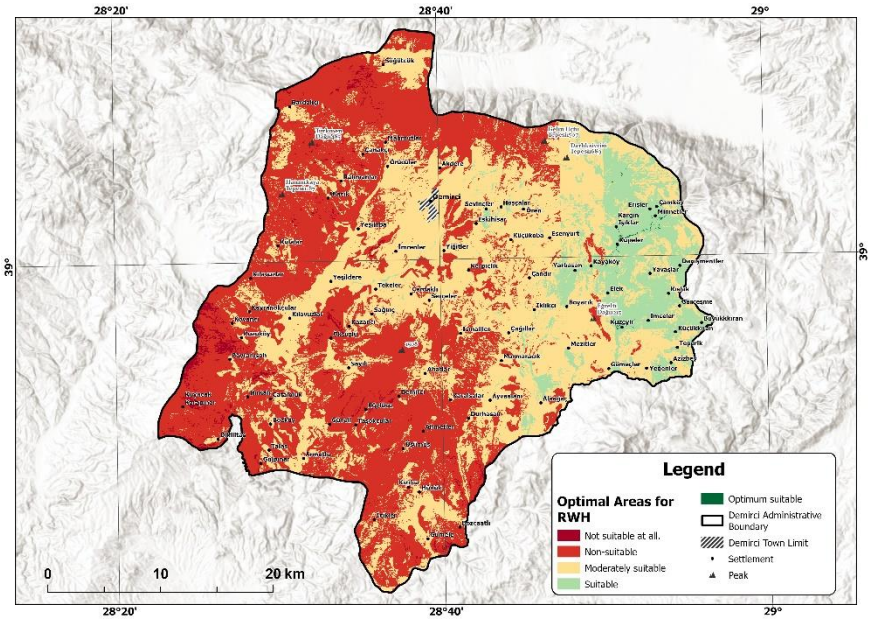



*Figure 5 Areas suitable for RWH*

During the 2020–2024 period, the mean TCI values for the study area were calculated to range from 43 to 49, while the VHI values ranged from 40 to 59. These results indicate that the drought conditions in the study area remained within the normal range (Bento et al., 2018). To investigate the relationship between the areas identified as optimal by the AHP and the drought indices, a Pearson correlation analysis was performed. The correlation coefficient between the optimal areas and VHI was calculated as $r = -0.112$, while that between the optimal areas and TCI was $r = -0.149$. These results indicate a negative but weak relationship between the areas identified as optimal for RWH and the drought indices. In other words, as the extent of areas identified as optimal for RWH increases, a limited decreasing trend is observed in the drought indicators. This finding suggests that the areas identified as optimal for RWH remain below the threshold associated with drought risk under normal conditions.

**Discussion**

In the study area, 52.74% of the total area was identified as suitable for RWH. This proportion is higher than that reported by Adham et al. (2018) for regions with similar geographical characteristics. In contrast, Al-Adamat et al. (2010) reported a lower proportion of suitable areas. This difference may be attributed to variations in the topographic and climatic characteristics of the respective study areas. In the present study, the areas identified as suitable for RWH were found to be predominantly concentrated on agricultural land, which is consistent with the findings reported by Dile et al. (2013). The weak negative relationships observed between the RWH suitability areas and the TCI and VHI drought indices are partially consistent with the findings of Vohland and Barry (2009) for arid and semi-arid regions. However, Dervash and Wani (2022) reported a stronger negative correlation between RWH areas and drought indices. This discrepancy may be attributable to differences

in moisture conditions, precipitation regimes, and soil characteristics among the study areas.

## Conclusion

This study demonstrates that the AHP method produces results consistent with those of similar studies in the literature for identifying suitable areas for RWH, highlighting its effectiveness for RWH suitability assessment. In particular, the relatively high weights assigned to climatic parameters such as precipitation and runoff potential are noteworthy and are consistent with findings reported in previous studies. However, the relatively weak relationship identified between the drought indices and RWH suitability areas may be attributed to the specific climatic characteristics of Demirci District. The findings are expected to contribute to the development of water management strategies in regions with similar geographical and climatic characteristics. Future studies should consider the application of dynamic modeling approaches, such as machine learning and deep learning, as well as the evaluation of additional climatic and drought-related parameters.

## Kaynakça

Adham, A., Sayl, K. N., Abed, R., Abdeladhim, M. A., Wesseling, J. G., Riksen, M., Fleskens, L., Karim, U., & Ritsema, C. J. (2018). A GIS-based approach for identifying potential sites for harvesting rainwater in the Western Desert of Iraq. *International Soil and Water Conservation Research*, *6*(4), 297–304. https://doi.org/10.1016/J.ISWCR.2018.07.003

Al-Adamat, R., Diabat, A., & Shatnawi, G. (2010). Combining GIS with multicriteria decision making for siting water harvesting ponds in Northern Jordan. *Journal of Arid Environments*, *74*(11), 1471–1477. https://doi.org/10.1016/J.JARIDENV.2010.07.001

Alotaibi, B. A., Baig, M. B., Najim, M. M. M., Shah, A. A., & Alamri, Y. A. (2023). Water Scarcity Management to Ensure Food Scarcity through Sustainable Water Resources Management in Saudi Arabia. *Sustainability (Switzerland)*, *15*(13). https://doi.org/10.3390/su151310648

Ammar, A., Riksen, M., Ouessar, M., & Ritsema, C. (2016). Identification of suitable sites for rainwater harvesting structures in arid and semi-arid regions: A review. *International Soil and Water Conservation Research*, *4*(2), 108–120. https://doi.org/10.1016/J.ISWCR.2016.03.001

Arnell, N. W., van Vuuren, D. P., & Isaac, M. (2011). The implications of climate policy for the impacts of climate change on global water resources. *Global Environmental Change*, *21*(2), 592–603. https://doi.org/10.1016/J.GLOENVCHA.2011.01.015

Bento, V. A., Gouveia, C. M., DaCamara, C. C., & Trigo, I. F. (2018). A climatological assessment of drought impact on vegetation health index. *Agricultural and Forest Meteorology*, *259*, 286–295. https://doi.org/10.1016/J.AGRFORMET.2018.05.014

Dervash, M. A., & Wani, A. A. (2022). *Climate change alleviation for sustainable progression*. CRC Press.

Dile, Y. T., Karlberg, L., Temesgen, M., & Rockström, J. (2013). The role of water harvesting to achieve sustainable agricultural intensification and resilience against water related shocks in sub-Saharan Africa. *Agriculture, Ecosystems & Environment*, *181*, 69–79. https://doi.org/10.1016/J.AGEE.2013.09.014

Hassan, W. H., Mahdi, K., & Kadhim, Z. K. (2025). GIS-based multi-criteria decision making for identifying rainwater harvesting sites. *Applied Water Science*, *15*(3), 45. https://doi.org/10.1007/s13201-025-02378-5

Kogan, F. N. (1995). Droughts of the late 1980s in the United States as derived from NOAA polar-orbiting satellite data. *Bulletin of the American Meteorological Society*, *76*(5), 655–668.

Mishra, S. K., & Singh, V. P. (2013). *Soil conservation service curve number (SCS-CN) methodology* (Vol. 42). Springer Science & Business Media.

Muratoglu, A. (2020). Grey water footprint of agricultural production: An assessment based on nitrogen surplus and high-resolution leaching runoff fractions in Turkey. *Science of The Total Environment*, *742*, 140553. https://doi.org/10.1016/J.SCITOTENV.2020.140553

Özben, O. M., & Güngör, M. (2024). Denizli Serinhisar ilçesi havzasında yağmur suyu hasadına uygun bölgelerin belirlenmesi. *Pamukkale Üniversitesi Mühendislik Bilimleri Dergisi*, *30*(5), 668–678. https://doi.org/10.5505/pajes.2023.85616

Radwan, F., & Alazba, A. A. (2023). Suitable sites identification for potential rainwater harvesting (PRWH) using a multi-criteria decision support system (MCDSS). *Acta Geophysica*, *71*(1), 449–468. https://doi.org/10.1007/s11600-022-00895-4

Saaty, T. L. (1977). A scaling method for priorities in hierarchical structures. *Journal of Mathematical Psychology*, *15*(3), 234–281.

Vohland, K., & Barry, B. (2009). A review of in situ rainwater harvesting (RWH) practices modifying landscape functions in African drylands. *Agriculture, Ecosystems & Environment*, *131*(3–4), 119–127. https://doi.org/10.1016/J.AGEE.2009.01.010


BİDGE